Analytical solution for chemical fluid injection into linear heterogeneous porous media based on the method of characteristics

Yangyang Qiao [a], Dimitrios Georgios Hatzignatiou [b],[*]

[a] *Karlsruhe Institute of Technology, Department of Civil Engineering, Geo and Environmental Sciences, Adenauerring 20b, Karlsruhe 76131, Germany*
[b] *University of Houston, Petroleum Engineering, 5000 Gulf Freeway, Houston TX 77204, USA*

ABSTRACT

Injection of Newtonian fluids in porous media to displace linearly another Newtonian fluid is described by the Buckley-Leverett (BL) fractional flow theory derived for incompressible, constant viscosity fluids at constant injection rate in a homogeneous and isotropic reservoir. Injection of non-Newtonian fluids can be addressed by modifying the fractional flow equation by considering the dependence of injected fluid viscosity with velocity, changes of residual oil saturation and chemical adsorption on rock. In this work, the BL fractional flow model is extended to describe injection of non-Newtonian fluids into a 1D linear heterogeneous formation accounting for fluid adsorption, permeability reduction, inaccessible pore volume, and presence of a denuded water bank developed over time ahead of non-Newtonian zone. Results from derived analytical solutions demonstrate fluids saturation and pressure drop across the formation, fluids production rate and cumulative volumes to be in close agreement with the ones from a commercial reservoir simulator.

1. Introduction

In a world of an ever-growing energy demand and economies built and strongly dependent on fossil fuels, it is generally acknowledged that crude oil produced from hydrocarbon-bearing reservoirs plays a major role as the leading source of energy. The development of an oil reservoir usually can be subdivided into three major stages: initial (primary) oil recovery resulted from the natural energy existing in the reservoir, secondary oil recovery associated with operations engaged to maintain the reservoir pressure and displace oil from the injection towards the production wells through water or gas injection after primary oil production declines, and finally tertiary oil recovery, often named enhanced oil recovery (EOR). In EOR processes, a wide array of specialized and advanced techniques such as miscible gas, chemicals (polymers or surfactants) and thermal energy injection can be used to produce additional oil after the end of a secondary process; the choice of the process used depends on both technical and economic constraints (Green and Willhite, 1998; Sorbie, 1991). In general, nearly 20–40 % of the initial oil in place can be extracted through the first two stages and the implementation of the EOR techniques can help to extract up to an additional around 20–30 % of the initial oil reserves in place. Chemical flooding is an important EOR method that has been used for more than 50 years to effectively recover remaining oil from the reservoir at the end of waterflooding. It uses water-soluble surfactant and/or aqueous polymer solutions engaged to increase the capillary number by decreasing oil/ water interfacial tension or decreasing the water/oil mobility ratio, respectively. The presence of these chemicals in the injected water influences the fractional flow curve through the relative permeability curves, residual oil saturation, and injected aqueous solution viscosity. The adsorption of these chemicals against the formation rock surface cause time-dependent alterations in their aqueous solution concentration along the distance between the injection and production wells.

Due to its technical and commercial viability, polymer flooding has been considered one of the most promising EOR technologies. Wang et al. (2001) reported an incremental oil production of up to 300,000 STB/D from a large-scale polymer flooding implemented in the Daqing oil field in China. Used polymers in the field can be either viscosifying polymers or viscoelastic polymers. Typically, the former will reduce the injected water mobility by increasing its viscosity, which will impact the fractional flow curve as discussed by Green and Willhite (1998) and Rossen et al. (2011). Hatzignatiou et al. (2013) used a commercial simulation model to conduct a simulation study to compare experimentally measured oil production and determine the polymer flow behavior in linear core samples. They also (Hatzignatiou et al., 2015) investigated the effects of core wettability on the displacement of oil in core samples. Several authors (Askarinezhad et al. 2017, 2018, 2021; Azad and Trivedi, 2018; Erincik et al., 2017; Huh and Pope, 2008; Lotfollahi et al. 2016; Qi et al., 2018; Song and Hatzignatiou, 2022) reported that the use of a secondary viscoelastic-polymer flood following a viscosifying polymer one reduces oil residual saturation, S_{or}, below the residual oil saturation, S_{orw} achieved from waterfloods in

Nomenclature

A	Cross-sectional area, m^2
A_p	Chemical adsorption, kg chemical /kg rock
$\widehat{C}_p$	Retained chemical, kg chemical /PV m^3
C_i	Concentration of species i, ppm
D_p	Retention factor, dimensionless
f	Fractional flow (water cut), fraction
k	Absolute permeability, m^2
k_j	Phase j effective permeability, m^2
k_{rj}	Phase j relative permeability, dimensionless
L	Porous medium linear length, m
M	End-point mobility ratio, dimensionless
n	Power-law exponent, relative permeability exponent, dimensionless
P	Pressure, Pa or atm
q	Volumetric flow rate, m^3/s
q_D	Dimensionless volumetric flow rate
R_i	Retained (adsorbed) amount of species i, chemical kg / rock kg
s_w or s_p	Water or polymer saturation, fraction
t	Time, s or min
t_D	Dimensionless time
u	Darcy velocity, m/s
v	Actual fluid velocity, m/s
x	Linear distance, m
x_D	Dimensionless linear distance

Greek Letters

α	Exponent of DPR fluids' properties
$\dot{\gamma}$	Shear rate, s^{-1}
λ	Critical time constant, s
μ	Viscosity, Pa.s
ρ	Density, kg/m^3
ρ_s	Rock density, kg/m^3
ϕ	Porosity, fraction

Subscripts

1	Formation domain (rock type) 1
2	Formation domain (rock type) 2
BT	Breakthrough time
D	Dimensionless
e	End point
f	Fluid or front
H	Hydrostatic
i	Species, initial, linear interval
ir	Irreducible
j	Linear bed number, phase
o	Oil
p	Polymer
pf	Polymer/oil front
r	Rock
w	Water
wb	Oil bank
wf	Water/oil front

Superscripts

0	Reference conditions
j	Linear bed number

---

laboratory experiments. Mechanisms which contribute to the observed reduced residual oil saturation include mobility control, improved sweep efficiency, and improved microscopic displacement efficiency. Therefore, for viscosifying polymers, there is another factor which affects the fractional flow curve, and this is the change of the relative permeability curves and residual oil saturation. In this work, the focus of the presented analytical solutions and the associated results will be on the injection of viscosifying polymers. The application of the second class of polymers, viscoelastic, and their impact on oil recovery in heterogeneous systems are addressed by Qiao and Hatzignatiou (2023).

2. Analytical solutions based on fractional flow theory for chemical flooding

For more than a half century, the Buckley–Leverett immiscible fluid displacement model has been used to simulate two-phase flow in porous media for one-dimensional homogeneous systems. Buckley and Leverett solved the immiscible fluid displacement problem using the fractional flow curve through which provided simple methods to define the sharp water saturation front position and to compute the water saturation profile in a porous medium containing oil which is displaced linearly by the injected water (Buckley and Leverett, 1942). Their initial model gives the water propagation velocity through the linear system where capillary pressure and gravity effects are ignored; later models have been also presented in the literature incorporating these effects. Calculating the average water saturation behind the water front, Welge (1952) established a relationship between the average water saturation as a function of either the total volume of water injected or the injection time. Both Buckley–Leverett theory and Welge equation considered only the injection of Newtonian fluids in the oil-saturated porous media. For the polymer flooding fractional flow curve, this is always represented by increasing the aqueous phase viscosity since the

polymer will generally transport in the aqueous phase (Ding et al., 2020). Green and Willhite (1998) discussed extensively the water- and chemical-injection in linear homogeneous oil-saturated porous media both as secondary and tertiary processes.

An extension of the analytical Buckley-Leverett solution incorporating the Welge (1952) technique for one-dimensional immiscible displacement of a Newtonian fluid by a non-Newtonian fluid in porous media was presented by Wu et al. (1991) and Wu (2016). The authors considered the non-Newtonian fluid viscosity to be a function of the flow potential gradient and phase saturation, and reported that the development of the injected fluid saturation profile and the displacement efficiency are controlled by the relative permeabilities and the inherent complexities of the non-Newtonian fluid. The authors verified the water saturation results from their analytical solution against results from a numerical model developed to simulate of flow of immiscible non-Newtonian and Newtonian fluids in porous media. Wu et al. (1993) also extended the Buckley-Leverett theory to the two-phase flow problem in one-dimensional linear systems which consists of two flow domains with different properties for the Newtonian fluids. The authors stated that the Buckley-Leverett analytical solution is still applicable in the composite system except that there is a saturation profile discontinuity induced by the flux transition across the interface between adjacent domains. Wu et al. (2010) also investigated the non-Darcy flow effects based on the Forchheimer and Barre-Conway models in both linear and radial composite porous media. Rossen et al. (2011) extended the fractional flow theory of two-phase flows to polymer flooding in one-dimensional cylindrical flow, where the polymer rheology varies with the distance of the injection well therefore the fractional flow curve is a function of position. A recent study conducted by Ding et al. (2020) reviewed the analytical modeling approaches of polymer flooding and surfactant flooding based on fractional flow theory in a homogeneous porous media and illustrated the effects of surfactant adsorption and
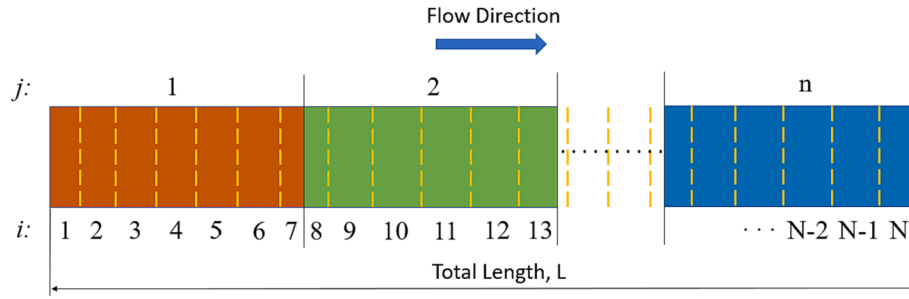
Fig. 1. Sketch illustrating how the computational intervals, i, are numbered in a system containing two linear beds. The yellow dashed lines refer to the displacing distance at different polymer/water saturations. The distance intervals are forced to generate at the boundary of the two domains. Note: *j* represents linear beds or domains and *i* refers to the number of computational intervals. (For interpretation of the references to colour in this figure legend, the reader is referred to the web version of this article.)

partition, interfacial tension, initial oil saturation, and injection slug size during surfactant flooding, and the effects of initial oil saturation, polymer viscosity and viscoelasticity, slug size, polymer inaccessible pore volume and retention in the process of polymer flooding. Based on the theory of polymer–oil fractional flow, Sun et al. (2019) calculated polymer injectivity in a multilayer reservoir where each layer is considered to be homogeneous porous medium.

However, other works mostly considered non-Newtonian fluid displacing Newtonian fluid in homogeneous porous media (Wu et al., 1991; Rossen et al., 2011; Sun et al., 2019; Ding et al., 2020) or Newtonian fluid displacing Newtonian fluid in a heterogeneous porous media (Wu et al., 1993; Wu, 2016). This work extends the Buckley-Leverett theory to non-Newtonian fluid injection in a linear heterogeneous porous media consisted of *n* parallel layers along the direction of oil displacement. Our consideration is one-dimensional linear flow of two immiscible fluids through *n* formation domains (rock types) having different rock properties (permeability, porosity, and relative permeability curves). Adsorption (retention) phenomena of the injected non-Newtonian fluid in the two formation rocks is also incorporated into the model. For simplicity, results of a two-phase, immiscible flow problem are considered in an incompressible composite system which consists of two formation domains (rock types) with each domain having different rock properties. The assumptions stated in Appendix A for the standard Buckley-Leverett model are used for each flow domain in this mathematical model, namely, (a) the system is one dimensional linear, (b) the capillary pressure and gravity effects are negligible, (c) fluids and rocks are incompressible, (d) the rock properties are constant in each domain, and (e) the fluid properties are constant in each domain at a given injection rate.

3. Fractional flow function

Although the use of fractional flow theory between water and oil is straightforward and well-established (Buckley and Leverett, 1942, Welge, 1952), the effects of the injected chemical fluid on either the relative permeability curves - surfactant injection - or viscosity changes of the injected fluid and its non-Newtonian fluid behavior – polymer injection - on the fractional flow curve need to be considered when using the oil/injected-fluid fractional flow function.

More specifically for polymer injection, there are available mathematical models that describe the relationship between shear stress and shear rate of non-Newtonian fluids, such as the power-law model, Carreau-type (Carreau, 1972) model, Herschel-Bulkley (Herschel and Bulkley, 1926) model and the Cross-Power law model. In this work, the two classical models of power-law and Carreau-type are engaged to account for the non-Newtonian fluid behavior and illustrate how they affect the fractional flow equation.

The power-law model (Ostwald, 1929) is described by the following relationship

$$\mu_p = K(\dot{\gamma})^{n-1} \tag{1}$$

where μ_p represents the apparent polymer viscosity, K is the power-law constant, n is the power-law exponent and $\dot{\gamma}$ is the shear rate. The Carreau model (Carreau, 1972) is described by the equation

$$\mu_p = \mu_\infty + (\mu_{pN} - \mu_\infty)\left[1 + (\lambda\dot{\gamma})^2\right]^{[(n-1)/2]} \tag{2}$$

where μ_{pN} and μ_∞ are the polymer viscosities at zero shear rate and infinite shear rate, respectively. The parameter $1/\lambda$ is the critical shear rate and n is the shear-thinning ($n < 1$) or shear-thickening ($n > 1$) index.

Assuming that the viscosity of the aqueous polymer solution depends on its interstitial velocity v_p (Rossen et al., 2011), we have

$$\mu_p = \mu_p^0\left(\frac{v_p}{v_p^0}\right)^{n-1} = \mu_p^0\left(\frac{q_t f_p}{\phi v_p^0 A s_p}\right)^{n-1} \tag{3}$$

where $v_p = \frac{u_t f_p}{\phi s_p} = \frac{q_t f_p}{\phi A s_p}$. Here, u_t is the total injection velocity corresponding to the total injection rate q_t. μ_p^0 denotes a reference polymer viscosity related to an interstitial velocity v_p^0. A and ϕ represent the cross-section area of the one-dimensional porous media and its porosity, respectively. s_p is the polymer solution saturation.

Rossen et al. (2011) incorporated Eq. (3) into the conventional fractional flow equation (Eq. (4))

$$f_p = \frac{q_p}{q_o + q_p} = \frac{\frac{kk_{rp}}{\mu_p}}{\frac{kk_{rp}}{\mu_p} + \frac{kk_{ro}}{\mu_o}} \tag{4}$$

and obtained the following fractional flow function

$$f_p = \left[1 + \frac{k_{ro}\mu_p^0}{k_{rp}\mu_o}\left(\frac{q_t f_p}{\phi v_p^0 A s_p}\right)^{n-1}\right]^{-1}. \tag{5}$$

Then Eq. (5) can be solved implicitly for the fraction flow using an iterative method.

In this work, we want to consider the effects of the residual resistance factor (RRF) and inaccessible pore volume (IPV) due to the polymer retention. Therefore, the general Darcy's equations for polymer and oil flow become as follows

$$q_p = A\frac{k/RRF \bullet k_{rp}}{\mu_p}\Delta P_{x_f}, q_o = A\frac{k \bullet k_{ro}}{\mu_o}\Delta P_{x_f} \tag{6}$$

and the interstitial velocity in Eq. (3) takes the form of

$$v_p = \frac{u_t f_p}{\phi(1-IPV)v_p^0 s_p} = \frac{q_t f_p}{\phi(1-IPV)v_p^0 A s_p} \tag{7}$$
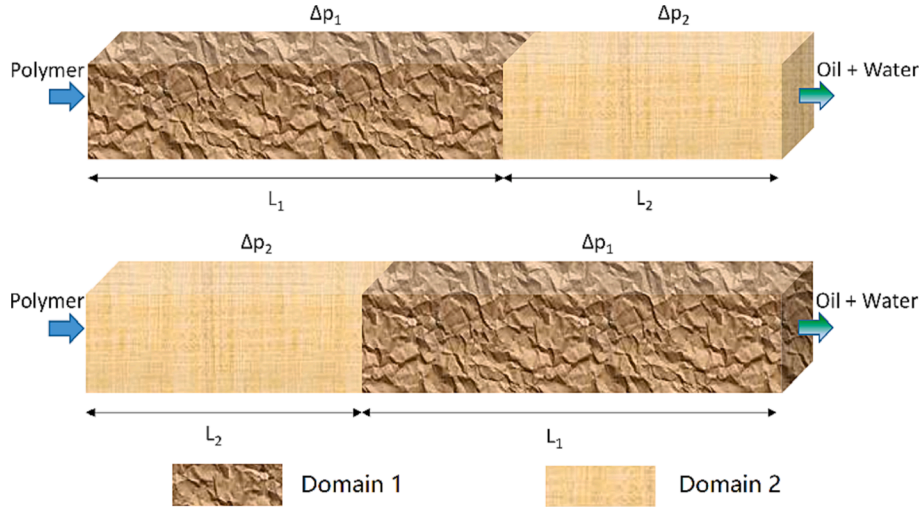
Fig. 2. Illustration of polymer solution injection into a composite one-dimensional system. The first case considers domain (bed) 1 on the injection (left side) of the formation and domain (bed) 2 on the effluent (right side). The second case considers the opposite scenario related to the two linear domains (beds).

Combining Eq. (3) and (4), the following fractional flow function can be obtained:

$$f_p = \left[1 + \frac{RRF k_{ro} \mu_p^0}{k_{rp} \mu_o} \left(\frac{q_t f_p}{\phi(1 - IPV) v_p^0 A s_p}\right)^{n-1}\right]^{-1}. \tag{8}$$

In Eq. (8), the aqueous polymer solution and oil phase relative permeabilities are given by

$$k_{rp} = k_{rp,e} (S_p)^{n_p}, k_{ro} = k_{ro,e} (1 - S_p)^{n_o} \tag{9}$$

with the normalized polymer saturation expressed as follows

$$S_p = \frac{S_p - S_{wi}}{1 - S_{wi} - S_{or}}. \tag{10}$$

In Eq. (9), $k_{rp,e}$ and $k_{ro,e}$ are the end-point values of relative permeabilities, respectively for polymer and oil phases. n_p and n_o are the Corey exponents. Similar to Eq. (5), the newly derived fractional flow function Eq. (8) considering RRF and IPV can also be solved through an iterative method. For the Carreau-type model shown in Eq. (2), a similar procedure can be adopted to get the implicit expression of fraction flow function.

Considering a heterogeneous formation composed of n distinct linear parallel beds across the flow direction (Fig. 1) with varying rock and fluid properties (permeability, porosity, initial water and residual oil saturations, and relative permeabilities), there will be n fractional flow equations given by Eq. (8), namely:

$$f_p^j = \left(\frac{1}{1 + \frac{RRF k_{ro} \mu_p^0}{k_{rp} \mu_o} \left(\frac{q_t f_p}{\phi(1 - IPV) v_p^0 A s_p}\right)^{n-1}}\right)^j \tag{11}$$

where the superscript $j (= 1, 2, ..., n)$ represents the linear bed j. Note that each linear bed has distinct rock and fluid properties, including polymer adsorption curves. Therefore, following the standard fractional flow (Buckley-Leverett) theory one needs to compute and construct all these fractional flow curves, draw the tangent lines from the corresponding initial points ($-D_{pj} + IPV_j, 0$) where D_p is the retention factor, and follow the appropriate fractional flow curves to determine the aqueous polymer solution (water) saturation distribution versus linear distance at a given time (Green and Willhite, 1998). Appendix A

includes relevant and important information pertaining to the water/oil Buckley-Leverett solution as well as a summarization of important relationships describing polymer flow in porous media. The detailed procedure to be followed to determine the aqueous polymer saturation versus linear distance for a two-zone linear composite system is outlined in Appendix B.

At a selected time, once the water saturation distribution versus linear distance has been determined, the pressure gradient, $(dp/dx)_i^j$, across the computational interval i of the linear bed j will be given by the following relationship:

$$\left(\frac{dp}{dx}\right)_i^j = \begin{cases} \frac{q_t}{A} \left(\frac{1}{\frac{\frac{k}{RRF} k_{rp}(S_p)}{\mu_p} + \frac{k k_{ro}(1-S_p)}{\mu_o}}\right)_i^j, & polymer - oil \ region \\ \\ \frac{q_t}{A} \left(\frac{1}{\frac{k k_{rw}(S_w)}{\mu_w} + \frac{k k_{ro}(1-S_w)}{\mu_o}}\right)_i^j, & water - oil \ region \end{cases} \tag{12}$$

Note that the total flow rate q_t and cross-sectional area A are the same for all n linear beds, and S_p represents the aqueous polymer saturation in the polymer invaded bed. Depending on the location of the polymer front, both or one of the two terms in the parenthesis on the right-hand side of Eq. (12) will be present in the calculation of the pressure drop across the bed. For example, if the polymer front has yet to reach bed j, only the right term will be present, whereas if the polymer front has passed entirely through the bed, only the left term will be required. Otherwise, both terms need to be accounted when calculating the pressure drop across the bed. The total pressure drop, Δp, across the entire linear heterogeneous formation can be determined by integrating the pressure gradient across the porous medium linear distance from 0 to L:

$$\Delta p = \int_0^{x_{pf}} \left(\frac{dp}{dx}\right)_i^j dx + \int_{x_{pf}}^{L} \left(\frac{dp}{dx}\right)_i^j dx$$

Model Input Parameters			
k_1 (mD)	300	$k_{rw1,e}$ (-)	0.5
k_2 (mD)	500	$k_{rw2,e}$ (-)	0.5
S_{wi1} (-)	0.25	$k_{ro1,e}$ (-)	0.8
S_{wi2} (-)	0.4	$k_{ro2,e}$ (-)	0.7
S_{or1} (-)	0.35	n_{w1} (-)	1.3
S_{or2} (-)	0.2	n_{w2} (-)	1.4
μ_w (cP)	1	n_{o1} (-)	2.5
μ_o (cP)	10	n_{o2} (-)	2.5
μ_p^0 (cP)	40	n (-)	0.9
q_t (cm^3/min)	0.5	L_1 L_2 (cm)	15.24
A (cm^2)	5.067	φ_1 (-)	0.2
P_{outlet} (atm)	1	φ_2 (-)	0.28

$$\cong \frac{q_t}{A} \sum_{i\ 1}^{i\ N_{pf}} \left(\frac{1}{\frac{k}{RRF} \bullet k_{rp}\left(S_p\right)}{\mu_p} + \frac{k \bullet k_{ro}\left(1\ S_p\right)}{\mu_o} \right)_i^j \Delta x_i + \frac{q_t}{A} \sum_{i\ N_{pf}+1}^{i\ N} \left(\frac{1}{\frac{k \bullet k_{rw}\left(S_w\right)}{\mu_w} + \frac{k \bullet k_{ro}\left(1\ S_w\right)}{\mu_o}} \right)_i^j \Delta x_i$$

$$(13)$$

In this work, we utilize an implicit expression of the fractional flow function to model polymer solution displacement of oil in a heterogeneous formation based on the method of characteristics (MOC). For simplicity, a composite system is used in the remaining of this work to illustrate the application of the proposed methodology and illustrate achieved results. The flow behavior of the injected chemical (polymer) solution is illustrated through various polymer injection scenarios by altering rock and fluids properties. Fluid saturation and pressure results across the linear heterogeneous formation obtained from the proposed analytical model are compared and verified against ones obtained from a numerical commercial simulator (CMG, 2022). Appendix B provides a detailed description and a step-by-step approach outlining how the

proposed analytical solution is applied for polymer flooding in a composite porous medium system.

4. Results and discussion

4.1. Linear composite model

In this section, a one-dimensional linear heterogeneous system with composite domains is used to display results obtained from the analytical solution for polymer injection into a core sample containing oil at irreducible water saturation. Fig. 2 shows the composite domains for two different cases. The first case and second case have each domain in the opposite direction. The polymer solution is injected from the left boundary of the composite system while the water and oil are produced from the right boundary. The input parameters used for the polymer flooding cases are summarized in Table 1. For simplicity in this paper, we assume polymer and water have same relative permeability curves, which means that $k_{rw,e}$ $k_{rp,e}$ and n_w n_p referring to Eq. (9).

4.2. Effect of formation heterogeneity on fractional flow curves

Fractional flow functions in the absence of gravitational and capillary forces are generally calculated using the traditional expression Eq. (4) provided the viscosities of the flowing phases are constant. Eq. (3) suggests that the polymer viscosity varies with its interstitial velocity thus, the modified fractional flow expression Eq. (8) can be used to calculate the polymer fractional flow f_p based on the chosen values of flow rates, RRF and IPV. More specifically, Fig. 3 displays two sets of fractional flow curves for a two-bed (domain) composite domain with different rock properties in each bed, using the input from Table 1. In this part of the work, the water $f_{wj}(j$ $1, 2)$ fractional flow curve is computed from the conventional expression of fractional flow function Eq. (4) and the polymer solution $f_{pj}(j$ $1, 2)$ fractional flow curves are computed from the modified expression of fractional flow function Eq. (8). In order to compare our results against the ones computed from a
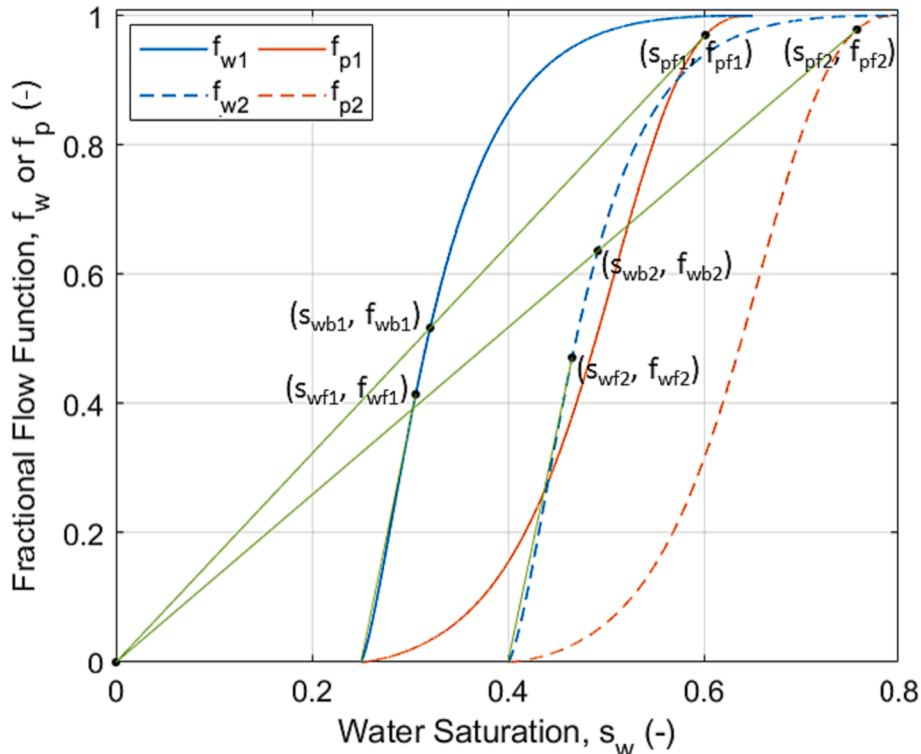
Fig. 3. Fractional flow curves of an aqueous phase (water or polymer solution) for a two-bed composite domain with negligible chemical adsorption.
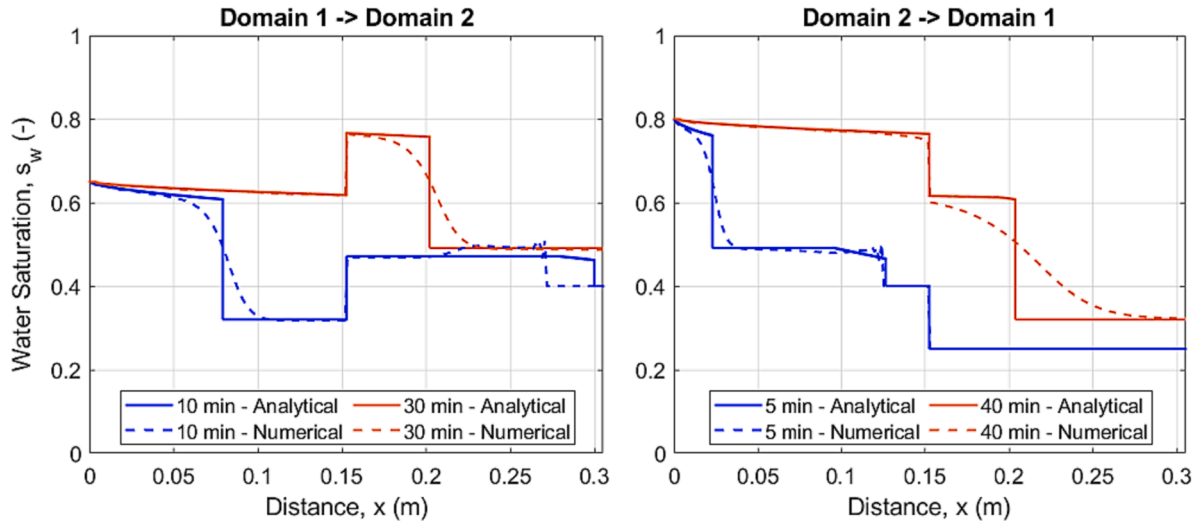
Fig. 4. Simulation results of analytical solution water saturation profile along the flooded oil-bearing porous medium compared against results from the numerical simulator CMG. The interface between the two linear domains (beds) is located at 0.1524 m.

commercial simulation model (CMG, 2022) that considers during oil displacement the polymer viscosity to be independent of polymer interstitial velocity, we used n ≈ 0.9 as the power-law index for the non-Newtonian polymer solution in Eq. (8) with a reference polymer solution viscosity of 40 cP, which is the value used in the simulator. One should note that there are three typical saturations for each domain: water saturation front S_{wfj}, oil bank water saturation S_{wbj} and polymer front saturation S_{pfj} where ($j \approx 1,2$). Note that the subscripts 1 and 2 represent domains 1 and 2, respectively, and subscript p refers to polymer solution. Note that for simplification, for the remaining of the paper, the subscript "p" in the polymer aqueous solution saturation will be replaced by "w" keeping always in mind that when discussing results for polymer, these are related to polymer aqueous solution saturation and not water saturation.

The tangents are drawn from the *(0, 0)* point – assuming there is no polymer retention – to the two polymer fractional flow curves wo define the polymer solution front $\left(S_{pfj}, f_{pfj}\right)$ and the oil bank points $\left(S_{wbj}, f_{wbj}\right)$ as shown in Fig. 3. The tangent from $\left(S_{wij}, f_{wij}\right)$ – here the subscript i pertains to the initial water saturation in the two domains – to the two water fractional flows define the waterfront $\left(S_{wfj}, f_{wfj}\right)$ points. When polymer adsorption is present, the tangents to the polymer fractional flow curves are drawn from ($-D_{pj}, 0$) when IPV is zero and from ($-D_{pj} + IPV_j, 0$) when IPV is not zero.

4.3. Results comparison - analytical solution versus numerical simulation

First, we compare and analyze results from synthetic experiments where the effects of polymer adsorption, permeability reduction (RRF) and inaccessible pore volume (IPV) are not considered into the analytical solutions. Subsequently, the polymer adsorption effects are included in the results provided. Finally, the combined effects of inaccessible pore volume and permeability reduction are also considered as a result of polymer adsorption in the porous media. The polymer flooding tests are conducted for two cases: one is for the forward flow from domain 1 to domain 2 and the other is for the reverse flow from domain 2 to domain 1. All results presented from the analytical solution include saturation profiles, pressure profile distribution, pressure drop across the formation, and cumulative oil/water production rates. These analytical results are compared with results obtained from the commercial simulation software CMG.

Fig. 4 shows a comparison of the analytical water saturation profiles (solid lines) against the numerical results (dashed lines) obtained from the commercial simulator CMG for a simple polymer flooding case
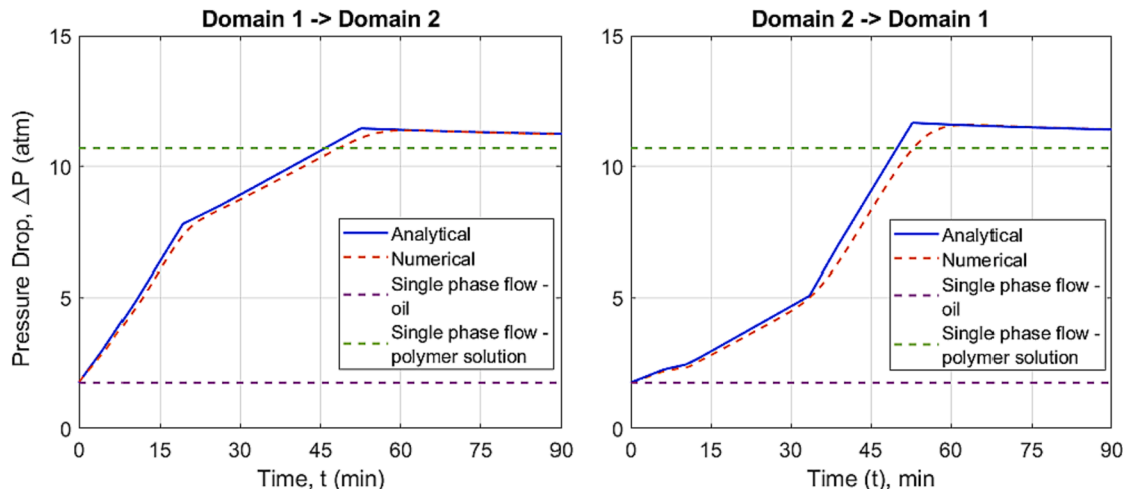
Fig. 5. Analytical pressure drop solution results along the entire domain displayed versus time and compared against numerical pressure drop results from CMG.
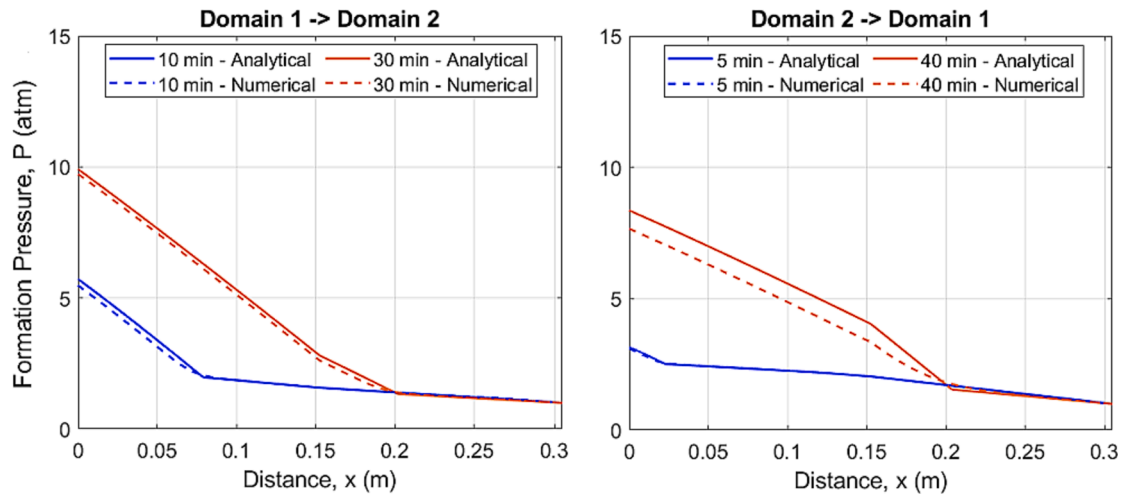
Fig. 6. Analytical versus simulation pressure profile displayed for selected times.
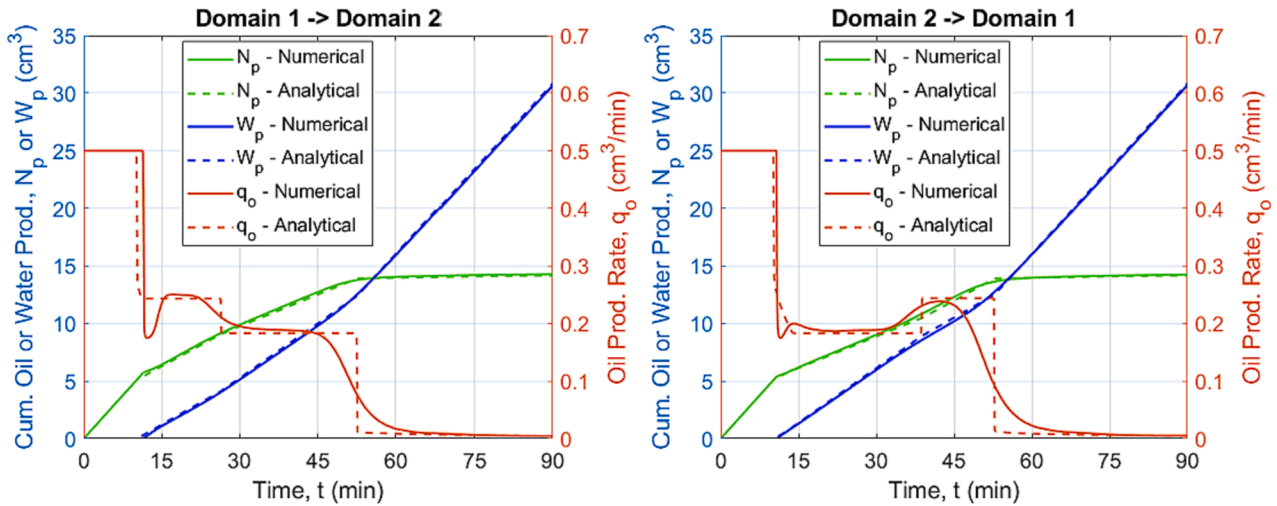
Fig. 7. Oil production rate and oil and water cumulative production versus time – comparison between analytical solution (dashed curves) and numerical solution (solid curves).

without accounting for the effects of polymer adsorption, permeability reduction and inaccessible pore volume. The left panel of Fig. 4 illustrates the saturation profiles across the formation for oil displacement from domain 1 to domain 2 and at specific times (10 min and 30 min). the boundary between domains 1 and 2 is clearly depicted by the observed water saturation jumps occurring at the domains' interface at linear distance of 0.1524 m from the formation inlet. It is noticeable that the analytical solution yields sharp saturation fronts for both the water and polymer fronts while the numerical results have relatively diffusive saturation fronts. It is also noticeable that the numerical water saturations at 10 min displays non-physical profiles in the oil bank region; this is also observed in the water saturation profiles at 5 min in the right panel of Fig. 4 where the polymer flooding is taking place from domain 2 to domain 1 (reverse flow compared to flow direction for the left panel of Fig. 4). In both cases (forward and reverse flow), one can observe the polymer and the oil bank regions at early times but only the polymer region at the later times. The results displayed in Fig. 4 clearly indicate that the analytical solutions presented in this work yield saturation profiles along the formation in close agreement with the ones obtained from numerical solutions.

For the same case as the one discussed in Fig. 4, Fig. 5 shows the pressure drop along the formation as a function of polymer solution injection time. As previously, the solid curves represent the simulation

results and the dashed curve the results from our analytical solutions. The two horizontal lines shown in Fig. 5 represent the pressure drop across the formation for single-phase oil flow (lower dashed line) and single-phase polymer solution flow (upper dashed line), respectively. Clearly, there are two major turning points in the pressure drop results presented in Fig. 5; the first point is when the polymer solution flows from the left domain to the right one and the second point refers to a time when polymer front breaks through the entire porous medium system (domain 2 outlet). The displayed pressure drop results in Fig. 5 show that there is a good agreement between the analytical and numerical solution except when polymer solution flows from domain 2 into domain 1. This is attributed to the differences observed between the analytical and numerical water saturation profiles (see saturation profiles at 40 min in Fig. 4). The same behavior is also observed in the second panel of Fig. 6 (see difference between 0.15 m 0.2 m) where the corresponding pressure profile along the system distance is plotted at given times. Note that in Fig. 6 the backpressure boundary condition of 1 atm is constrained at the outer boundary pressure of the system.

Fig. 7 demonstrates the comparison of oil production rate, cumulative oil and water production results between the analytical solution and the numerical one. Despite the fact that numerical oil rate results display similar behavior with the water saturation when compared to analytical ones, the cumulative (average) oil production values are approximately
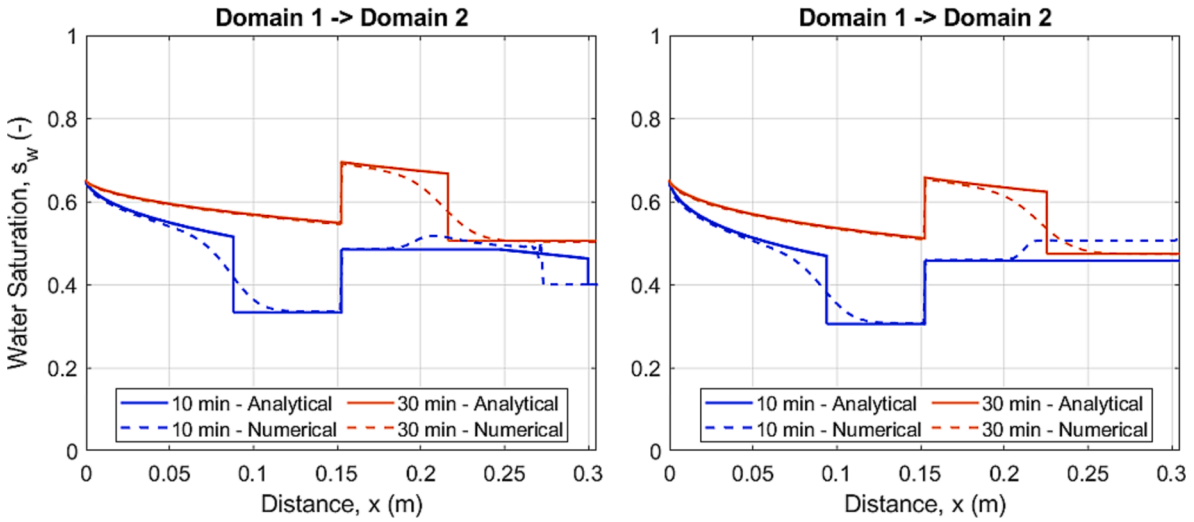
Fig. 8. Analytical solution water saturation profile along the flooded oil-bearing porous medium compared against results from the numerical simulator CMG. Left panel: polymer viscosity 5 cP and oil viscosity 10 cP. Right panel: polymer viscosity 5 cP and oil viscosity 20 cP. The interface between the two linear domains (beds) is located at distance 0.1524 m from formation inlet and the flow is from domain 1 to domain 2.
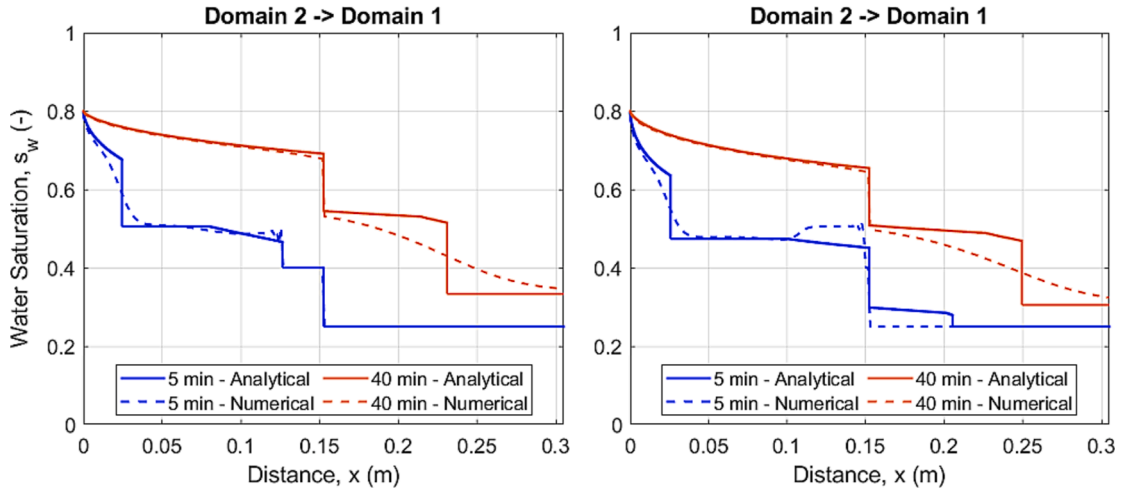
Fig. 9. Analytical solution water saturation profile along the flooded oil-bearing porous medium compared against results from numerical simulator CMG. Left panel: polymer viscosity 5 cP and oil viscosity 10 cP. Right panel: polymer viscosity 5 cP and oil viscosity 20 cP. The interface between the two linear domains (beds) is located at distance 0.1524 m from formation inlet and the flow is from domain 2 to domain 1.

the same as the analytical results in both flow directions (left and right panels in Fig. 7). Moreover, there is also a very good match between the analytical and numerical results for the cumulative water production curves for both forward flow (domain 1 to domain 2) and reverse flow (domain 2 to domain 1).

4.3.1. Fluids viscosity effects

In order to validate more cases between analytical and numerical results, the viscosities of oil and polymer solution are varied. The first case examined is with 5 cP polymer solution and 10 cP oil and the second one refers to a 5 cP polymer solution and 20 cP oil. Figs. 8–11, respectively, display the water saturation profiles vs. system distance and pressure drops vs. time for the forward and the reverse flow directions. Compared to the results shown in the left panel of Fig. 4 the polymer viscosity has a lower value 5 cP in the corresponding left panel of Fig. 8; these results show that in both analytical and numerical solutions the polymer fronts move faster while the locations of the water front are the same despite the marked difference in the polymer front saturation between the two cases. Note also that the oil bank size is bigger in Fig. 8 compared to the one displayed in Fig. 4. Furthermore,

the numerical solution seems to give different fluctuations on the saturation profiles in the oil bank region when polymer viscosity is changed from 40 cP to 5 cP, a behavior that is not observed in the analytical solution. In the right panel of Fig. 8, a higher oil viscosity value (20 cP) is used. Compared to the left panel of the same Fig., it is seen that the polymer front in the analytical solution has a lower saturation value since the oil mobility decreases. The numerical solution follows the same saturation trend as the analytical one in the polymer invaded portion of the formation, whereas the difference between them is relatively large in the oil bank region as we can see the blue dashed line has an increasing trend at distance around 0.2 m which stabilizes at stabilizes at distance approximately 0.22 m. For the reverse flow from domain 2 to domain 1, the comparisons of saturation profiles are shown in Fig. 9 where the overall trend looks acceptable between the analytical and numerical solutions. We omit the detailed explanation for the difference between them since this follows a similar behavior as the forward flow illustrated in Fig. 8.

Corresponding to saturation profile displayed in Fig. 8 and Fig. 9, the pressure drops across the formation (Δp p_{in} p_{out}) versus time are shown in Fig. 10 and Fig. 11. These figures show five typical turning
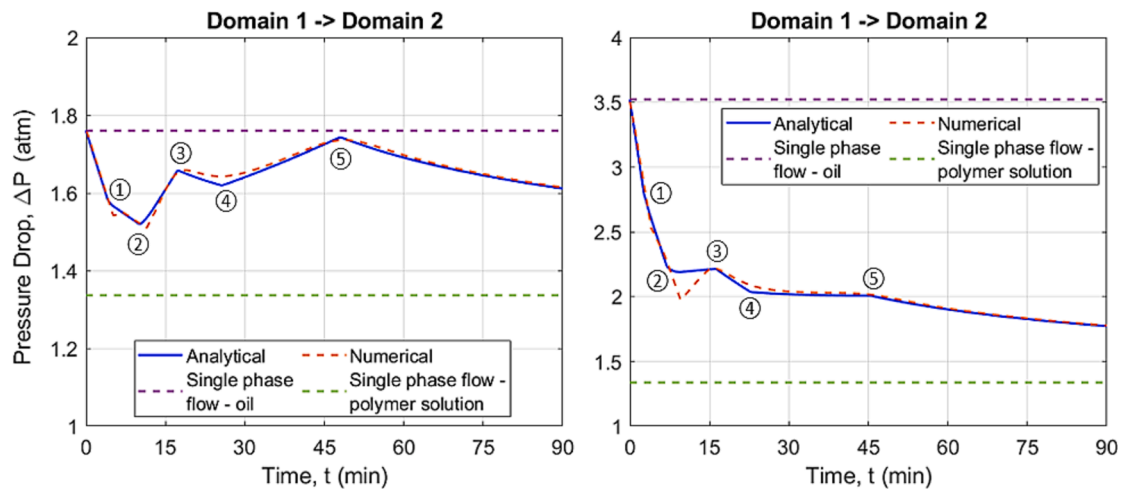
Fig. 10. Formation pressure drop analytical solution results along the entire domain displayed versus time and compared against numerical obtained from CMG simulator. Left panel: polymer viscosity 5 cP and oil viscosity 10 cP. Right panel: polymer viscosity 5 cP and oil viscosity 20 cP. Polymer injection is from domain 1 to domain 2.
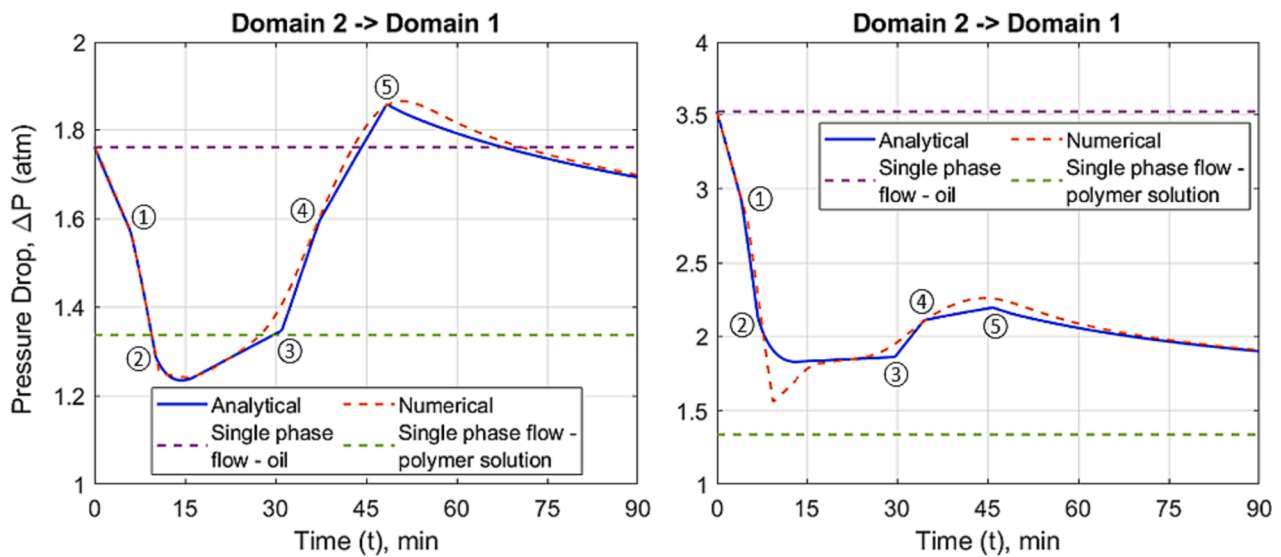
Fig. 11. Formation pressure drop analytical solution results along the entire domain displayed versus time and compared against numerical results obtained from the CMG simulator. Left panel: polymer viscosity 5 cP and oil viscosity 10 cP. Right panel: polymer viscosity 5 cP and oil viscosity 20 cP. Polymer injection is from domain 2 to domain 1.

points in pressure drop curves as numbered in Fig. 10. The first one occurs when the waterfront reaches domain 2 at time 4.4 min left and 2.7 min right, and the second one when water breaks through at the production end of the formation (t_{BTw} 10.5 min left and 7 min right). The third and fifth Δp turning points take place when polymer front enters into domain 2 (17.5 min left and 16.3 min right) and when it breaks through at the production end of the formation (t_{BTp} 48 min left and 45.8 min right). As it is shown in Fig. B.6 (line A2D2), an extra water bank shock wave with a higher saturation value is generated when polymer enters into domain 2. The fourth point in Fig. 10 means that additional water shock wave passes by the right boundary (outlet) of the system. The overall comparison of pressure drop across the formation versus time shows that the proposed analytical solution has a very good agreement with the numerical ones albeit some minor differences primarily due to numerical dispersion effects of the simulation results. It should be noted that in Fig. 5 the polymer viscosity is relatively high (40 cP), therefore there are two distinct inflection points on the pressure-drop vs. time graph reflecting the location of polymer front.

Similar to the forward injection case results shown in Fig. 10, the pressure drop across the formation for the reverse flow also contains five typical inflection points as illustrated in Fig. 11. The explanations for this behavior are the same as the ones presented earlier for the forward injection case: points 1 and 2 reflect the waterfront arrival at the interface between domain 1 and domain 2, and the waterfront break-through at the outer boundary of system, respectively. Points 3 and 5 represent the polymer front reaching the domain-1/domain-2 boundary and the polymer front breakthrough at the outer boundary of the formation, respectively. Finally, the inflection point 4 is related to an extra water bank shock-wave (low oil saturation) generated when the polymer enters into domain 1; see line A1C1 in Fig. B.10. Fig. 11 shows an acceptable agreement between analytical and numerical formation pressure drop results.

4.3.2. Effects of residual resistance factor (RRF) and inaccessible pore volume (IPV)

Polymer retention in a porous medium can result in permeability
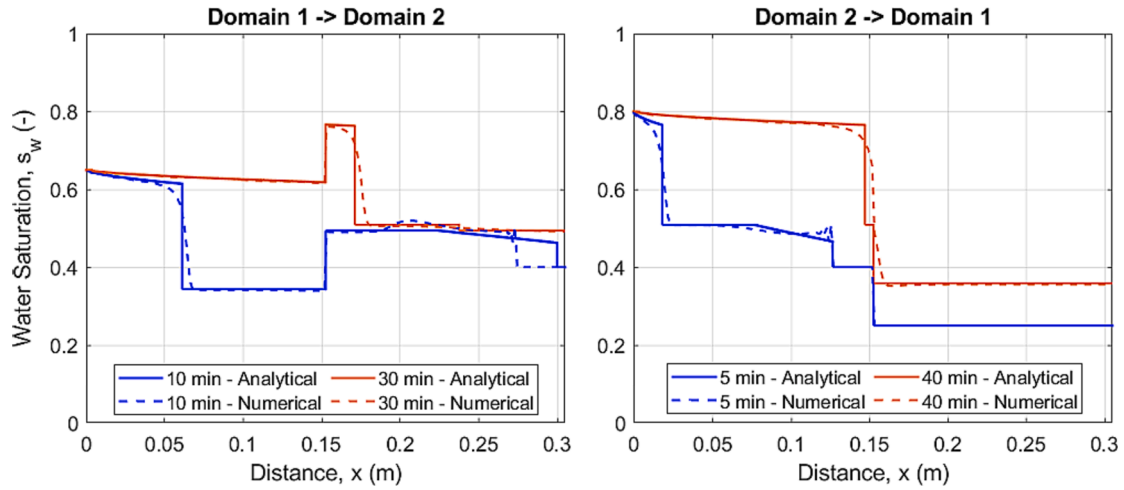
Fig. 12. Simulation results of analytical solution water saturation profile along the flooded oil-bearing porous medium compared against results from the numerical simulator CMG, $D_{pj} = 0.18$ and $RRF_j = 1$ for both domains.
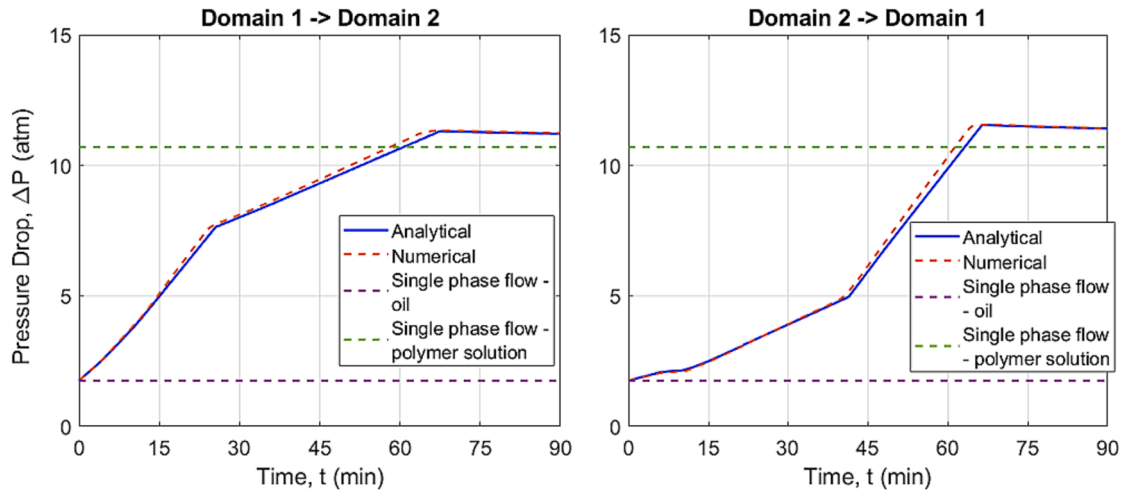
Fig. 13. Analytical solution of formation pressure drop results along the entire domain displayed versus time and compared against numerical pressure drop results from CMG, $D_{pj} = 0.18$ and $RRF_j = 1$ for both domains.

reduction (residual resistance factor - RRF) and inaccessible pore volume (IPV) of the polymer flooded formation. Therefore, it is essential to consider the effects of polymer retention (adsorption, mechanical and hydrodynamic entrapment) during polymer flooding on both fluid saturation distribution and pressure drop across the formation. Following Green and Willhite (1998), an adsorption coefficient D_{pj} (j denotes the number of linear bed/domain) is introduced to account for polymer retention on the developed analytical model; please refer to Appendix A for more details. Note that commercial reservoir simulation software, such as CMG, consider a dynamic isothermal process for polymer retention (adsorption) requiring polymer adsorption input data in the form of Langmuir curves. Compared to the case of polymer flooding without adsorption displayed in Fig. 4, two observations are noticeable in Fig. 12 which shows the computed water saturation profiles in the porous media accounting for polymer adsorption. Note that permeability reduction in both domains due to polymer retention was assumed to be negligible (RRF_j 1). The positions of water fronts are the same in both cases, whereas the polymer fronts, as expected, move relatively slower in the polymer flood showing in Fig. 12 due to polymer adsorption, which can also to some extent narrow the diffusive parts of polymer front region.

The corresponding pressure drops versus time for the case of polymer

adsorption water saturation profiles depicted in Fig. 12 are plotted in Fig. 13. A comparison of Figs. 5 and 13 shows that the pressure drop in the absence of polymer adsorption builds up faster than the one with polymer adsorption, although the overall trend of the formation pressure drop curves and the final plateau values are practically the same between the no-adsorption and adsorption cases. In addition, Fig. 5 shows that the numerical solution yields a slightly slower pressure drop buildup in the absence of polymer adsorption. The reason for this behavior can be captured in the saturation profiles (Fig. 4) where diffusive polymer fronts result in a lower pressure drop compared to the sharp polymer front generated by the analytical solution. These pressure drop differences between two solution approaches are enhanced as time increases. Interestingly, in the presence of polymer adsorption (Fig. 12), numerical solutions yield diffusive polymer fronts which are relatively faster than the analytical ones at later times; see polymer front differences at 30 min from domain 1 to domain 2 and at 40 min from domain 2 to domain 1 polymer flooding. Therefore, the analytical solutions with polymer adsorption result in a relatively slower pressure drop buildup compared to the numerical ones (Fig. 13). The key reason causing this phenomenon is the implementation of dynamic polymer adsorption in the commercial simulator versus the constant polymer adsorption coefficient included in the analytical solution.
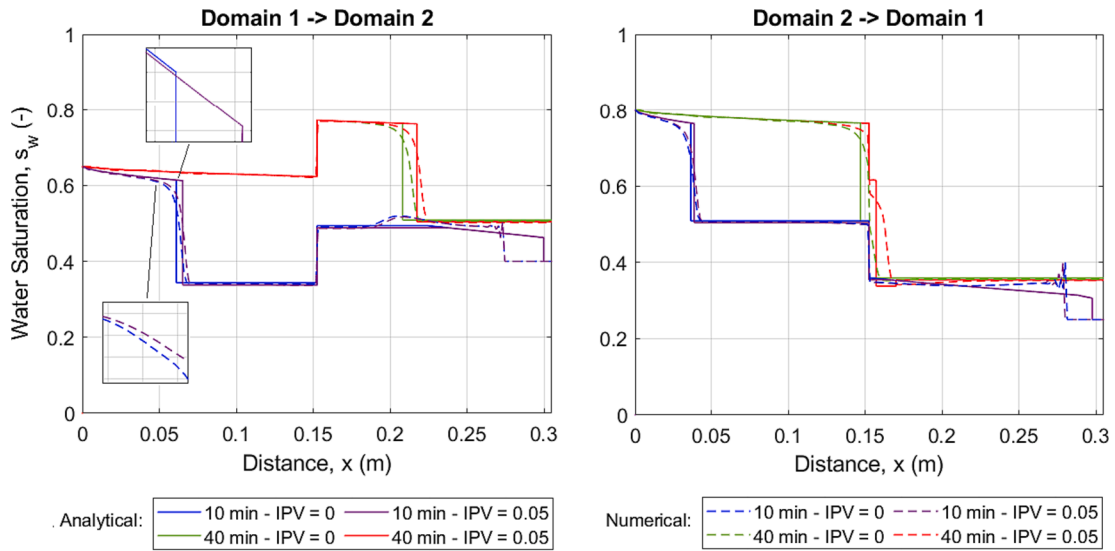
Fig. 14. Analytical solution water saturation profile along the flooded oil-bearing porous medium compared against results from numerical simulator CMG, with and without the effects of IPV.

Effects of Inaccessible Pore Volume (IPV): Unlike water, polymer molecules are not able to flow through the entire pore volume due to their size difference and blocked pores as a result of retained (adsorbed) polymer. The fraction of total pore volume, which is not available for polymer invasion is called inaccessible pore volume (IPV). Comparing to results displayed in Fig. 4 for the case of polymer flooding in the absence of IPV (i.e., IPV 0), the effects of IPV on water saturation profiles are illustrated in Fig. 14 where both cases with IPV and without IPV are compared. The IPV values considered for both domains are 5 %. Note that in this section, we use the same case as the one illustrated in Fig. 12 as the base case, which means that polymer adsorption is always present without permeability reduction (RRF_j 1).

The solid lines in Fig. 14 display water and polymer saturation results from the analytical solutions and the dashed lines are the corresponding results from the numerical simulator. As expected, this figure shows that a 5 % IPV in both domains results in a faster polymer front movement for both analytical and numerical solutions. From a mathematical point of view, estimation of polymer front saturation and its velocity needs to be based on the tangent line drawn from point (IPV D_p, 0); please refer to

Appendix B for further details. In addition to causing a relatively lower water saturation values in the oil bank region, IPV also causes a relatively lower polymer front saturation and faster front velocities. This can be further enhanced by the fact that IPV impacts polymer fractional flow curves (f_p increases with an increasing IPV value; see Eq. (11)). IPV does not affect the shape of polymer fronts either diffusive (numerical) or sharp (analytical) fronts; it only accelerates polymer front propagation through polymer-flooded porous media. The differences on saturation profiles due to IPV effects are very comparable between the analytical and the numerical solutions (Fig. 14). In addition, at time t 10 min from domain 1 to domain 2 polymer flood, we use zoomed-in plots to compare the differences of polymer profiles between the analytical and numerical solutions. The polymer profile changes induced by IPV in the analytical solution emanates from the fractional flow function. The numerical solution shows a different behavior, i.e., lower polymer saturation profiles with a slower polymer front movement. Note that the overall fit between the analytical and numerical solutions is satisfactory except that the non-physical profiles (oscillations) in the numerical oil
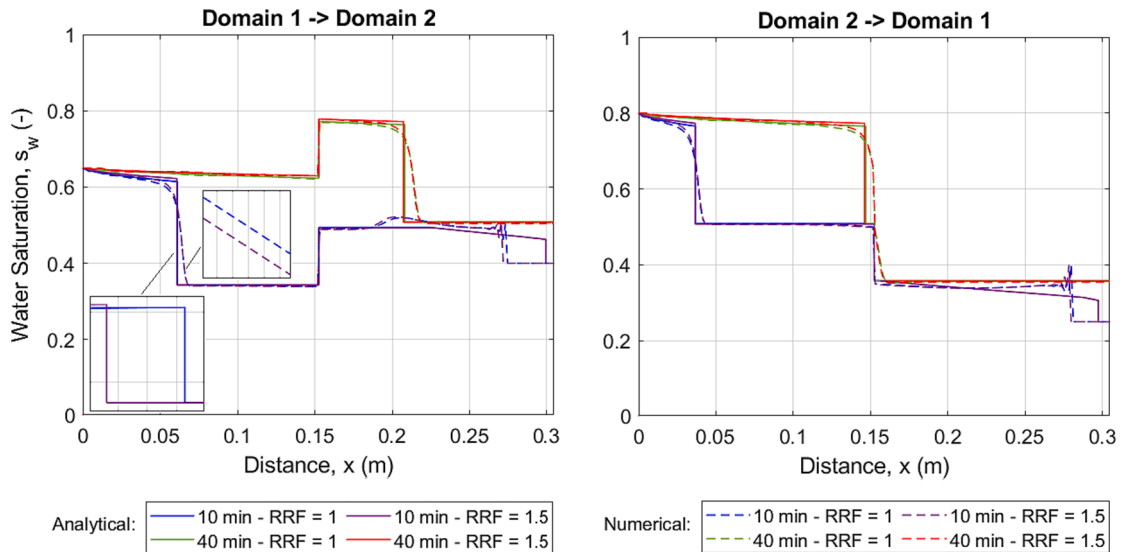
Fig. 15. Analytical solution water saturation profile results along the flooded oil-bearing porous medium compared against results from the numerical simulator CMG, with and without the effect of RRF.
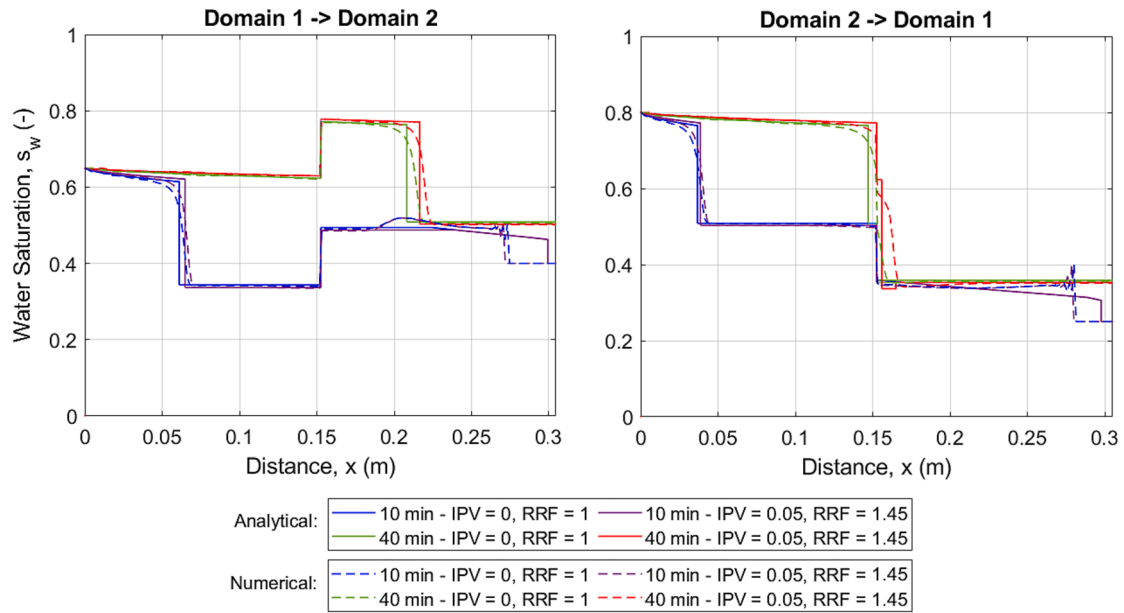
Fig. 16. Simulation results of analytical solution water saturation profile along the flooded oil-bearing porous medium compared against results from the numerical simulator CMG, with and without the combined effects of IPV and RRF.

bank are still present as observed previously for the results presented in Fig. 4.

Effects of Residual Resistance Factor (RRF): One important outcome of polymer adsorption/ retention in the porous medium is the reduction in rock's permeability (RRF). Considering a negligible IPV (reduction of the portion of pore space polymer flows through the flooded medium due to polymer retention) in both domains, Fig. 15 illustrates the effect of polymer reduction (RRF_j 1.45 for both domains) on the water saturation profiles at times 10 min and 40 min. Zoomed-in plots for both analytical and numerical solutions at time t 10 min are included for the case of polymer flooding from domain 1 to domain 2. From these plots it is observed that the polymer front saturation in both analytical and numerical solutions is slightly higher and its velocity slower when RRF 1.45 compared to the RRF 1 case. However, the results presented in Fig. 15 clearly show that there are no significant

variations on the saturation profiles, analytical and numerical, when polymer adsorption with an associated permeability reduction is accounted for. The minor differences observed in the saturation profiles caused by the presence of RRF can be explained by the fact that f_p decreases with increasing RRF as indicated by Eq. (11) that includes the RRF effects in the linear beds (domains) of the heterogeneous flooded oil-bearing formation. The corresponding results with RRF 1.45 have a lower water saturation in the oil bank, a higher polymer front saturation, a faster polymer front velocity after the tangent line is drawn to the polymer fractional flow curves, which can be verified by the results illustrated in Fig. 15. The differences on the polymer saturation profiles resulted from RRF 1.45 and RRF 1 are similar between the analytical and numerical solutions. Moreover, in the analytical solutions RRF has no impact on the region near the waterfront, whereas different RRF values can result in some minor changes in the numerical solutions;
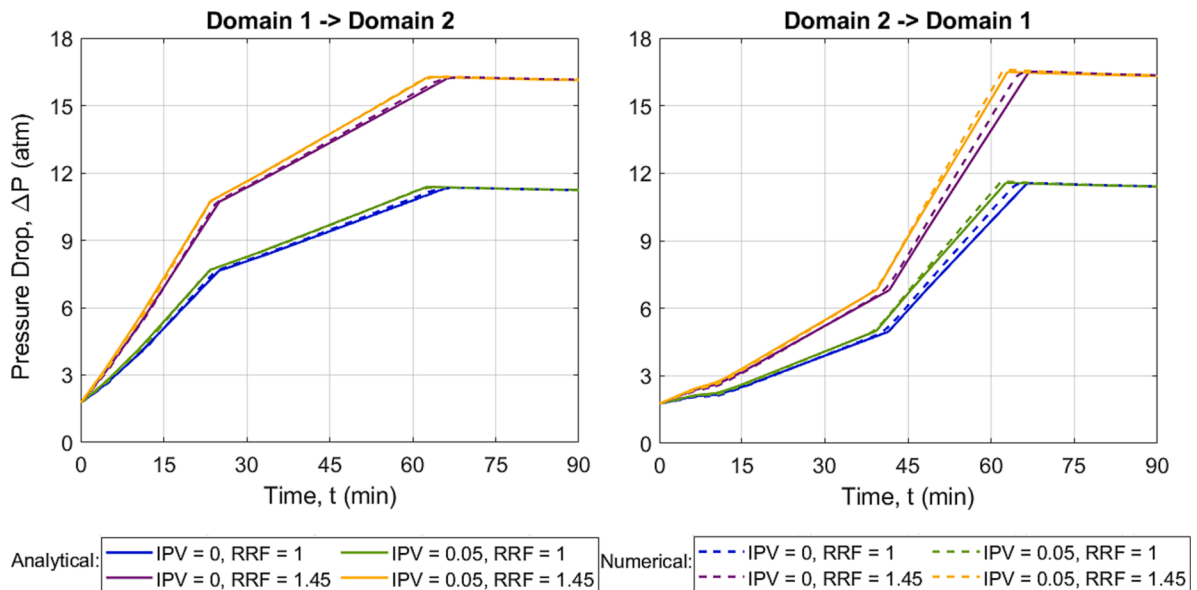
Fig. 17. Analytical solution for formation pressure drop across the formation displayed versus time and compared against numerical pressure drop results obtained from the CMG simulator in the absence and presence of IPV and RRF effects.
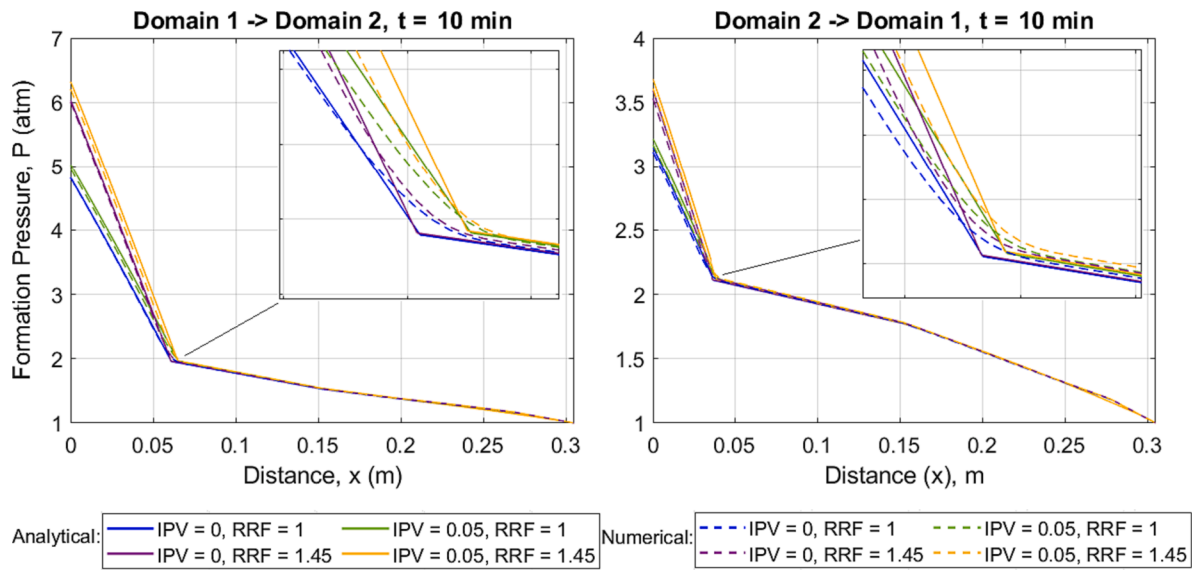
Fig. 18. Analytical versus simulation formation pressure profile displayed at time t = 10 min in the presence and absence of IPV and RRF effects.

see the non-physical oscillations at t = 10 min.

Effects of Inaccessible Pore Volume (IPV) and Residual Resistance Factor (RRF): This subsection considers the effects of both inaccessible pore volume and permeability reduction in the linear beds during polymer flooding. Therefore, Fig. 16 combines these two IPV and RRF effects, as shown in Fig. 14 and Fig. 15 respectively, and compares the results with the case without IPV and RRF effects illustrated in Fig. 12. Obviously, as expected, the results in Fig. 16 are an overlay of the results in Fig. 14 and Fig. 15. A very small piece of evidence of this is the difference in the water bank saturation profiles (at 10 min) vanishes in Fig. 16 based on the numerical results from domain 1 to domain 2. For either analytical or numerical solutions, the main differences caused by both effects on saturation profiles are still mainly dominated by the IPV as in Fig. 14.

The corresponding formation pressure drop curves versus time are shown in Fig. 17. As it has been observed in Figs. 4 and 6, pressure drop is strongly affected by the presence of the polymer flooded region. IPV impact on the pressure drop is through the accelerated polymer movement (see Figs. 14 and 16), therefore yielding higher pressure drops due to longer polymer propagation distance (see x_{pf} in Eq. (13)) compared to the case with IPV = 0. RRF has a minor impact on the saturation profiles

as shown in Fig. 15, but it reduces the permeability of the polymer swept regions and thus contributes to high pressure drops as illustrated in Eq. (13). In other words, IPV affects the rate of pressure drop buildup, whereas RRF influences the magnitude of pressure drop at the given polymer region, see Fig. 17 for details. Irrespectively of the IPV value used (with or without IPV), larger RRF values always result in a higher pressure drop in both forward and reverse flow directions in Fig. 17. The ratio of final plateau values between the cases with $RRF_j = 1$ and $RRF_j = 1.45$ is around 1.45 for both numerical and analytical solutions. This is because at the end of the polymer flood (after 70 min), polymer has already passed through the entire porous medium flooded domains and the pressure drop along the entire system is primarily dominated by polymer which has efficiently recovered the mobile oil, i.e., normalized polymer saturation close to 1. In contrast to RRF, IPV gives no impact on the final plateau values but only on the evolution speed of pressure drop before the polymer has broken through the entire heterogeneous system. This is an outcome associated with the polymer front moving faster in the flooded porous medium when the IPV values of the two domains are equal to 5 % (Fig. 16).

The corresponding pressure distribution profiles with zoomed-in plots are shown in Fig. 18 and Fig. 19 at two given times (10 min and
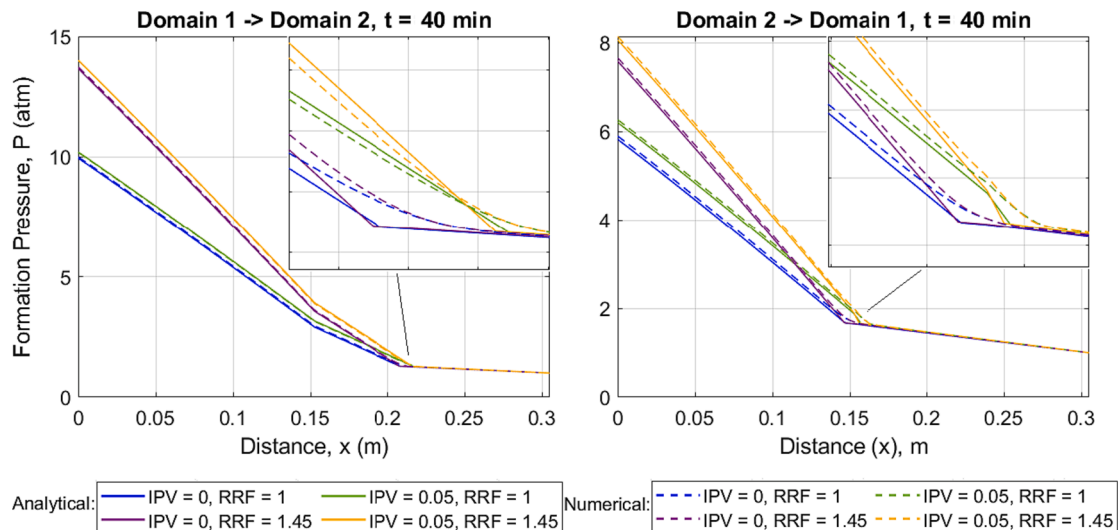
Fig. 19. Analytical versus simulation formation pressure profile displayed at time t = 40 min in the presence and absence of IPV and RRF effects.

Domain 1 -> Domain 2
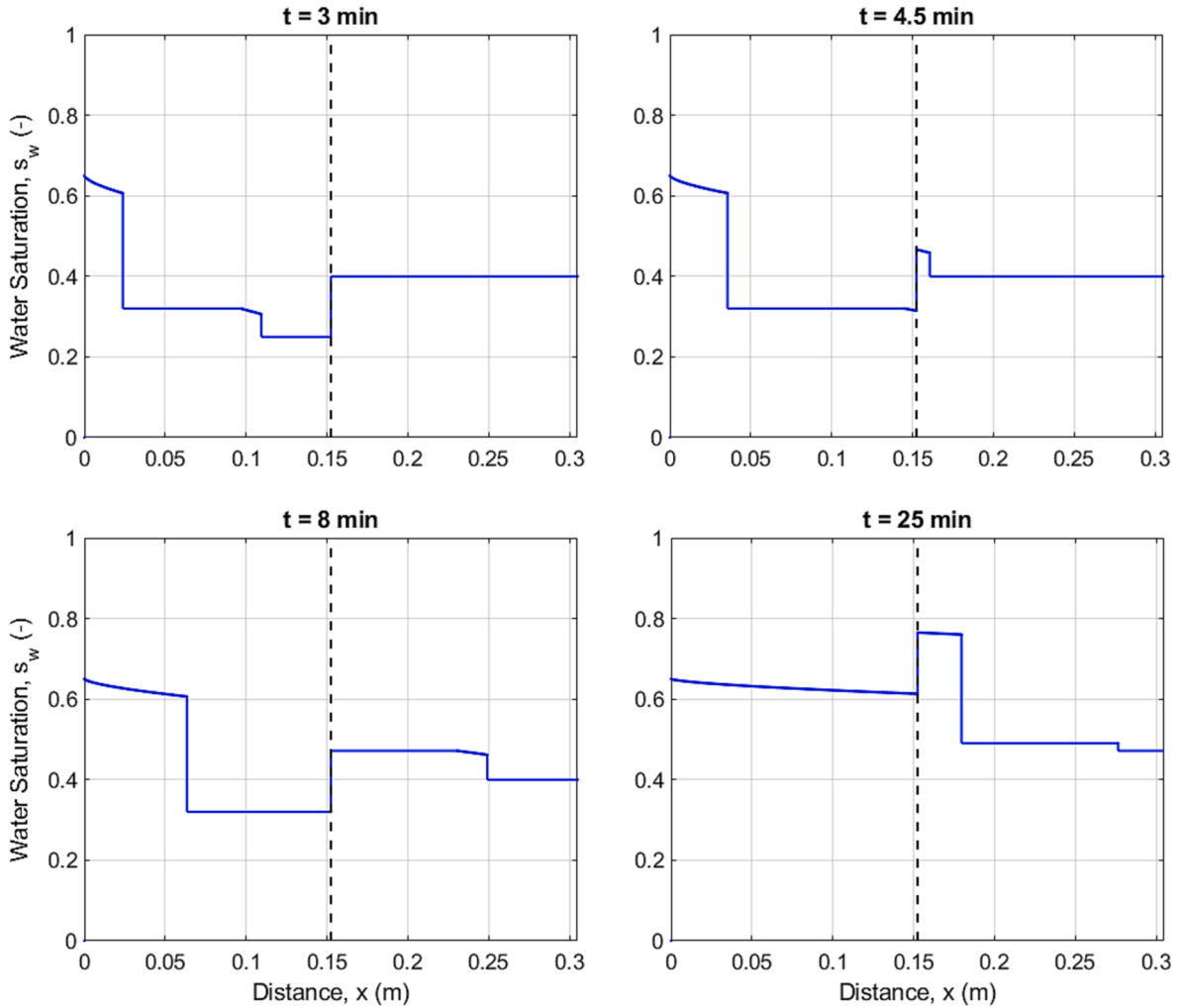
Fig. 20. Analytical solution of water saturation profiles along the entire porous medium domain (fluid flow from domain 1 to domain 2) at four different injection times.

40 min) for the cases shown in Fig. 16. Like Fig. 6, the outer boundary of system is constrained at pressure of 1 atm. From these two figures one can see the formed oil bank in all four cases yields practically the same pressure drop; however, polymer IPV and RRF effects cause differences in the observed pressure drop. Two groups of formation pressure drops are shown, one for RRF_j 1 and the other one for RRF_j 1.45. For these two sets of formation pressure drops, the IPV value of 5 % in both domains just yields some small differences compared to those without IPV effect. In particular, the ratio of the slope of pressure curves with RRF_j 1.45 to the slope with RRF_j 1 is 1.45 in the polymer region. Meanwhile, the faster polymer fronts caused by IPV 5 % result in a relatively larger high-slope curves due to the size of the polymer region, which can be clearly observed in the zoomed-in plot of Fig. 19. Therefore, our key observations can be summarized as follows: (a) IPV proportionally accelerates the polymer movement as well as the rate of pressure drop buildup, and (b) RRF proportionally enhances the pressure drop magnitude or the slope of pressure distribution of polymer regions without dramatically influencing the saturation profiles.

From Figs. 17 to 19, both analytical and numerical solutions follow the above statements when IPV and RRF are considered with the corresponding results to be quite close to each other. However, as shown in Fig. 17, in the absence of IPV effects, the numerical solution results are always faster than the analytical ones. This is similar to the behavior

shown in Fig. 13 where only adsorption is considered. We explained this by the fact that numerical polymer fronts are faster than the analytical ones. After consideration of IPV, the difference of pressure drop between the numerical and the analytical solutions is reduced in Fig. 17 and this can be referred to the impact of IPV on the polymer fronts shown in both Fig. 14 and Fig. 16. These Fig.s show that the polymer fronts in the analytical solutions catch up with the numerical ones when IPV 0.05. Another clear difference is illustrated in the zoomed-in plots of Fig. 18 and Fig. 19, which show the numerical solutions to be smoother in the polymer front part than the analytical ones due to the diffusive nature of the estimated polymer front shapes (see Fig. 16).

5. Saturation profile

In this section, we will show the how the saturation profile evolves with time for the two different situations shown in Fig. 2. As it is seen in Fig. 20, saturation profiles are illustrated at four typical stages, i.e., before the water front breakthrough the domain 2 (t 3 min); variable water front part in domain 1 has a dynamic transition to the domain 2 (t 4.5 min); all variable water saturation passes through the interface of domains followed by a constant water bank saturation (t 8 min); the polymer front in domain 1 will finally reach to domain 2 (t 25 min). The reverse case flowing from domain 2 to domain 1 is shown in Fig. 21
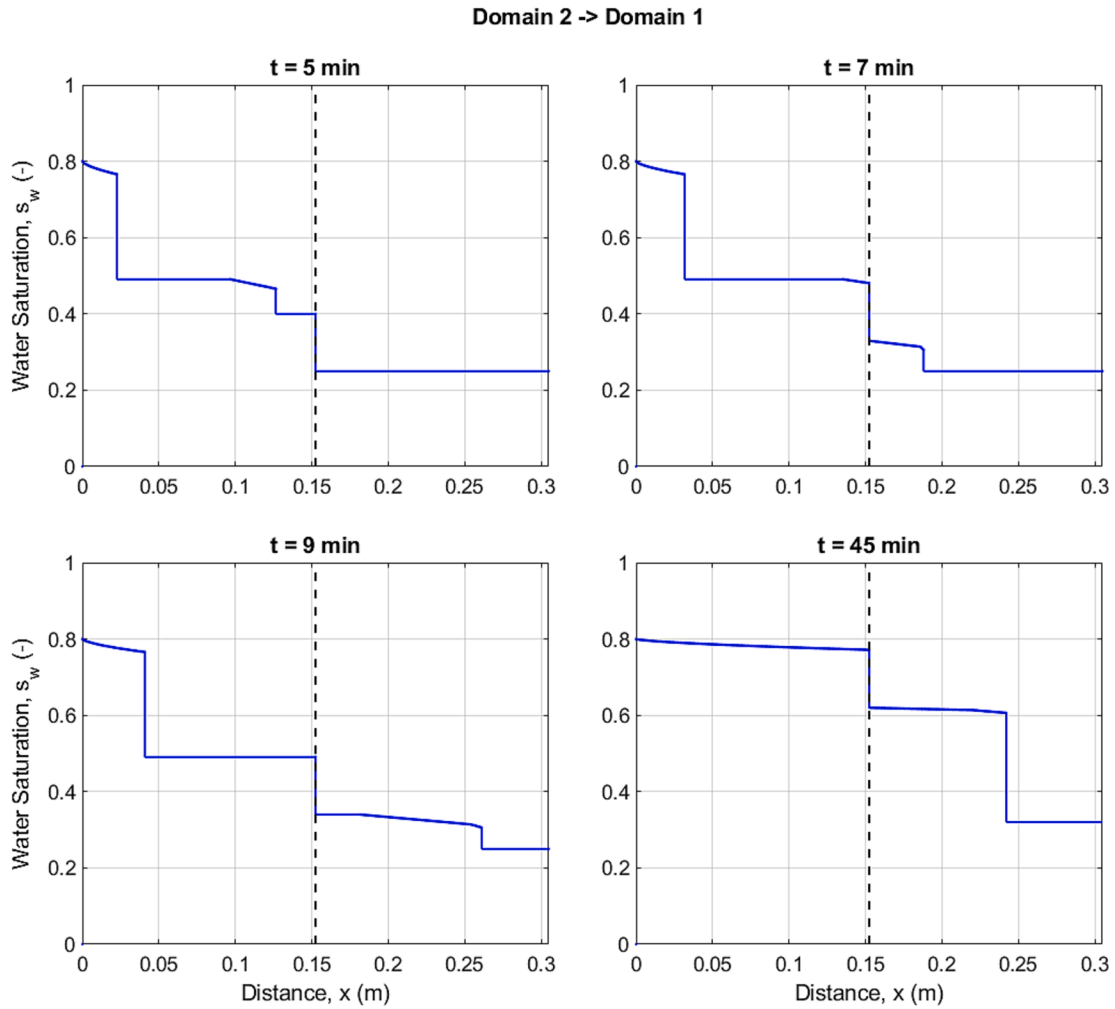
Domain 2 -> Domain 1

Fig. 21. Analytical solution of water saturation profiles along the entire porous medium domain (fluid flow from domain 2 to domain 1) at four different injection times.

where four different stages of saturation profiles are depicted similarly to Fig. 20.

There are some differences between these two cases in Fig. 20 and Fig. 21, especially when the fluid passes through the domain interface. We want to emphasize that all saturations passing through the domain interface should follow the conservation rule, i.e., $f_{w1}|_{S_{w1}} \quad f_{w2}|_{S_{w2}}$. This is the principle how the new saturation S_{w1} or S_{w2} is formed in the second domain (Wu, 2016). Appendix B provides a detailed description on the development and application of the presented analytical solutions.

6. Conclusions

This work introduces an analytical approach to obtain solutions – fluid saturations and pressure profiles as well as pressure drop across the flooded formation – for polymer flooding (oil displacement by injected polymer solution) in an oil-bearing heterogeneous porous medium consisted of n linear domains (beds) each having different and distinct rock and fluid flow properties. Results obtained from a heterogeneous composite system are provided and a step-by-step procedure is described to illustrate the application of the presented solutions. The analytical model presented considers the effects of polymer adsorption, inaccessible pore volume and permeability reduction in each one of the n linear domains (beds). In addition, the dynamic viscosity of the injected non-Newtonian fluid due to fluid velocity variation is also accounted for in

the construction of the polymer fractional flow curves required for the application of the solution procedure as outlined. The new fractional flow function includes the effects of polymer interstitial velocity, and as mentioned above, the inaccessible pore volume and permeability reduction. The analytical results presented include water saturation profile, pressure distribution in the porous formation, pressure drop across the formation, and cumulative oil or water rates and oil or water flow rates. These analytical results are computed, compared and verified by comparisons with the numerical results from the commercial software CMG. In view of a rather good agreement between analytical and numerical results, it is concluded that the proposed analytical solutions can be applied to obtain robust oil displacement performance results when a chemical fluid is injected into a linear, oil-bearing heterogeneous formation.

Declaration of Competing Interest

The authors declare that they have no known competing financial interests or personal relationships that could have appeared to influence the work reported in this paper.

Data availability

No data was used for the research described in the article.

Appendix A. – Formulations for water injection and polymer injection

A.1 - Classical Buckley-Leverett solution

The Buckley-Leverett (1942) model for one-dimensional, linear, two-phase flow in porous media yields the injected fluid saturation as function of position and time. The assumptions involved with the standard Buckley-Leverett solution are: (a) 1D linear flow in a horizontal reservoir with a constant cross section area, A; (b) immiscible flow of two incompressible fluids (e.g., water and oil); (c) homogeneous, isotropic, and incompressible formation (constant porosity, ϕ, and absolute permeability, k); (d) negligible capillary pressure; (e) initial wetting phase (water) saturation at irreducible conditions ($S_o = 1-S_{wi}$), and (f) constant injection rate of wetting phase (displacing fluid) at the formation inlet and fluid (oil and water) production at the formation outlet.

Denoting with q the constant volumetric injection rate, incompressibility of fluids implies that the total fluid flow rate across any cross-section of the reservoir will be equal to q. Darcy velocity, u, defined as $u = q/A$ is used conveniently in all equations given below. Fluid properties needed to formulate relevant equations are fluids viscosities, μ_w for water and μ_o for oil. In addition, phase relative permeabilities must be specified as a function of phase saturation.

Invoking the assumptions stated above, the mass balance equations for the water and oil phases can be written as follows:

$$\frac{\partial}{\partial x}\left(\frac{kk_{rl}}{\mu_l}\frac{\partial p}{\partial x}\right) = \phi\frac{\partial S_l}{\partial t}, \quad l = o, w \tag{A.1}$$

where S_l is the phase saturation, k the absolute permeability, ϕ the rock porosity, μ_l and k_{rl} are the phase l viscosity and relative permeability, respectively, and the subscript l represents either the oil or water phase.

Introducing the phase l mobility:

$$\lambda_l = \frac{kk_{rl}}{\mu_l}, \quad l = o, w \tag{A.2}$$

Eq. (A.1) can be rewritten as:

$$\frac{\partial}{\partial x}\left(\lambda_l\frac{\partial p}{\partial x}\right) = \phi\frac{\partial S_l}{\partial t}, \quad l = o, w \tag{A.3}$$

Adding the two-phase equations and considering the constraint $S_o + S_w = 1$ yields:

$$\frac{\partial}{\partial x}\left(\lambda_t\frac{\partial p}{\partial x}\right) = 0, \quad where \quad \lambda_t = \lambda_o + \lambda_w \tag{A.4}$$

The total fluid velocity given by:

$$u_t = -\lambda_t\frac{\partial p}{\partial x} \tag{A.5}$$

is constant and independent of the linear position x. Defining the phase fluid fluxes (Darcy velocities) by

$$u_l = -\lambda_l\frac{\partial p}{\partial x}, \quad l = o, w \tag{A.6}$$

and considering that the total flux is $u_t = u_w + u_o$, Eq. (A.5) can be rewritten as

$$\frac{\partial p}{\partial x} = -\frac{u_t}{\lambda_t}. \tag{A.7}$$

Eliminating the pressure term in the mass conservation equation for water using Eq. (A.7), the mass balance of water is expressed by:

$$u_t\frac{\partial}{\partial x}\left(\frac{\lambda_w}{\lambda_t}\right) + \phi\frac{\partial S_w}{\partial t} = 0 \tag{A.8}$$

The fractional flow term is expressed in the form:

$$f_w = \frac{q_w}{q_o + q_w} = \frac{\frac{kk_{rw}}{\mu_w}}{\frac{kk_{rw}}{\mu_w} + \frac{kk_{ro}}{\mu_o}} = \frac{\lambda_w}{\lambda_t}, \tag{A.9}$$

and thus Eq. (A.8) can be rewritten as:

$$u_t\frac{\partial f_w}{\partial x} + \phi\frac{\partial S_w}{\partial t} = 0 \tag{A.10}$$

This is the Buckley-Leverett (BL) equation. It is convenient to use BL equation in dimensionless form by defining the dimensionless position, x_D, and

dimensionless time, t_D, as follows:

$$x_D \quad \frac{x}{L} \tag{A.11}$$

$$t_D \quad \frac{u_t t}{\phi L} \tag{A.12}$$

Substituting these dimensionless variables in Eq. (A.10), results in the following dimensionless BL equation:

$$\frac{\partial S}{\partial t_D} + \frac{\partial f}{\partial x_D} \quad 0 \tag{A.13}$$

Supressing the subscript D in the Eq. (A.13) dimensionless terms for convenience purposes yields

$$\frac{\partial S}{\partial t} + \frac{\partial f}{\partial x} \quad 0 \tag{A.14}$$

Considering the dependence of fractional flow with the wetting phase saturation, the dimensionless Buckley-Leverett equation (Eq. (A.14)) can be written as:

$$\frac{\partial S}{\partial t} + f'(S)\frac{\partial S}{\partial x} \quad 0 \tag{A.15}$$

Suppose that there exists a unique solution for $S \quad S(x,t)$ for Eq. (A.15), let $g \quad [x(t), t]$ be a smooth curve in the x-t plane and use the single argument function $h(t) \quad S(x(t), t)$. Differentiating h with respect to t, one obtains

$$\frac{dh}{dt} \quad \frac{\partial S}{\partial t} + \frac{\partial S}{\partial x}\frac{dx}{dt} \tag{A.16}$$

Assuming the characteristic curve g satisfies the relationship

$$\frac{dx}{dt} \quad f'(S), \tag{A.17}$$

it follows that

$$\frac{dh}{dt} \quad \frac{\partial S}{\partial t} + f'(S)\frac{\partial S}{\partial x} \quad 0. \tag{A.18}$$

Eq. (A.18) implies that along the characteristic curve the saturation will maintain a constant value. According to Eq. (A.17), the curve on which S is constant, equal to S_0, is given by

$$x(t) \quad x_0 + f'(S)t \tag{A.19}$$

Since the initial solution $S(x,0) \quad 0$, Eq. (A.19) becomes

$$x(t) \quad f'(S)t \tag{A.20}$$

A.2 - Solution for polymer injection

For the transportation of polymer component with a constant total injection rate, q, the mass transport equation is given by (Green and Willhite, 1998):

$$\frac{\partial(S_p C_p)}{\partial t} + \frac{1 \quad \phi}{\phi}\frac{\partial(\rho_s A_p)}{\partial t} + \frac{q}{A\phi}\frac{\partial(f_p C_p)}{\partial x} \quad 0 \tag{A.21}$$

This equation can be further rewritten as:

$$S_p\frac{\partial C_p}{\partial t} + C_p\frac{\partial S_p}{\partial t} + \frac{\partial \widehat{C}_p}{\partial t} + \frac{q}{A\phi}\left[f_p\frac{\partial C_p}{\partial x} + C_p\frac{\partial f_p}{\partial x}\right] \quad 0 \tag{A.22}$$

where:

$$\widehat{C}_p \quad \frac{1 \quad \phi}{\phi}\rho_s A_p \tag{A.23}$$

denotes polymer retention on the rock in terms of the PV of the rock, ρ_s is the density of rock and A_p is the adsorption concentration of the polymer component in the rock.

Combining with the transportation equation of polymer solution, it follows:

$$\frac{\partial S_p}{\partial t} + \frac{q}{A\phi}\frac{\partial f_p}{\partial x} = 0 \tag{A.24}$$

Combining Eq. (A.24) and Eq. (A.22) one obtains:

$$\left[S_p + D_p\right]\frac{\partial C_p}{\partial t} + \frac{qf_p}{A\phi}\frac{\partial C_p}{\partial x} = 0 \tag{A.25}$$

where the chemical retention factor D_p is defined as:

$$D_p = \frac{\partial \widehat{C}_p}{\partial C_p} \tag{A.26}$$

In addition to adsorption effect, considering inaccessible pore volume (IPV), the pore volume that is accessible to polymer is ($\phi S_p - \phi$IPV). A material balance over the polymer yields:

$$\left[S_p + D_p - IPV\right]\frac{\partial C_p}{\partial t} + \frac{qf_p}{A\phi}\frac{\partial C_p}{\partial x} = 0 \tag{A.27}$$

The velocity of the polymer front can thus be calculated from:

$$v_p|_{S_p = S_{pf}} = \frac{q}{A\phi}\frac{f_p}{S_p + D_p - IPV}\Big|_{S_p = S_{pf}} \tag{A.28}$$

The velocity of a given polymer saturation S_p^* behind the polymer front can be expressed as follows:

$$v_p|_{S_p^*} = \frac{q}{A\phi}\frac{df_p}{dS_p}\Big|_{S_p^*} \tag{A.29}$$

Appendix B. - Calculation details for a composite formation

B.1 - Solution procedure

Step 1: Calculate the fractional flow curves for the two domains – Given an injection rate, the water–oil and the polymer-oil fractional flow curves for each domain are computed using Eq. (8).

Step 2: Identify the three critical points for each domain – For each domain, three important points need to be identified based on the Welge (1952) graphical technique, which are associated with: (a) the water–oil front saturation and corresponding water–oil fractional flow value $\left(S_{wf}, f_{S_{wf}}\right)$, (b) the oil bank water saturation and corresponding water–oil fractional flow value $\left(S_{wb}, f_{S_{wb}}\right)$, and (c) the polymer-oil front saturation and corresponding polymer-oil fractional flow value $\left(S_{pf}, f_{S_{pf}}\right)$. The water–oil front $\left(S_{wf}, f_{S_{wf}}\right)$ point is determined form the tangent line drawn from $(S_{wi}, 0)$ to the water–oil fractional flow curve; note that in this work we assume that the initial water saturation in the formation is equal to the irreducible water saturation, $S_{wi} = S_{wir}$. The polymer-oil front point $\left(S_{pf}, f_{S_{pf}}\right)$ is determined from the tangent line drawn from (IPV $- D_p, 0$) to the polymer-oil fractional flow curve. Finally, the $\left(S_{wb}, f_{S_{wb}}\right)$ point is determined as the intercept point of the line drawn from (IPV $- D_p, 0$) to the polymer-oil fractional curve and the water–oil fractional curve.

Step 3: Determine the saturation profile.

In this step, we will mainly focus on the water part due to its higher complexity than the polymer part which can follow the similar description for water when it flows to the second domain.

Saturation profile in the first domain - Compare the values of S_{wf} and S_{wb} to check if there is any variation part of water saturation.

Flow flux translation from first domain into the second one - When the injected fluid flows from the first (upstream) domain to the second (downstream) domain, the following continuation rule should be satisfied:

$$(f_w)_1 = (f_w)_2 \tag{B.1}$$

and the corresponding saturations will have translation from the first domain to the second domain.

Saturation profile in the second domain – There are two cases that need to be distinguished for the water saturation part.

Case 1. *When the water saturation front reaches the interface of two domains, if the fractional flow value is larger than the BL front fractional flow $f_{S_{wf}}$ in the second domain's water–oil fractional curve, an extra saturation profile will be generated starting from the time when the waterfront passes the interface of two domains.*

Case 2. *If not, there will be two kinds of situation. The first will be the constant fractional flow flux into the second domain. In this case, the previous saturation in the first domain will be translated to a new saturation in the second domain and the velocity of the front should obey the rule of jump condition (Eq. (B.2)). The second situation is a changing saturation profile flowing into the second domain, which will lead to an evolution of the water saturation front in the second domain and the front will keep being caught up until the front saturation goes to BL front saturation S_{wf} of the second domain. The reason for this process is due to the slower front velocity calculated based on the jump rule compared to the faster velocities of nearby saturations behind the waterfront.*
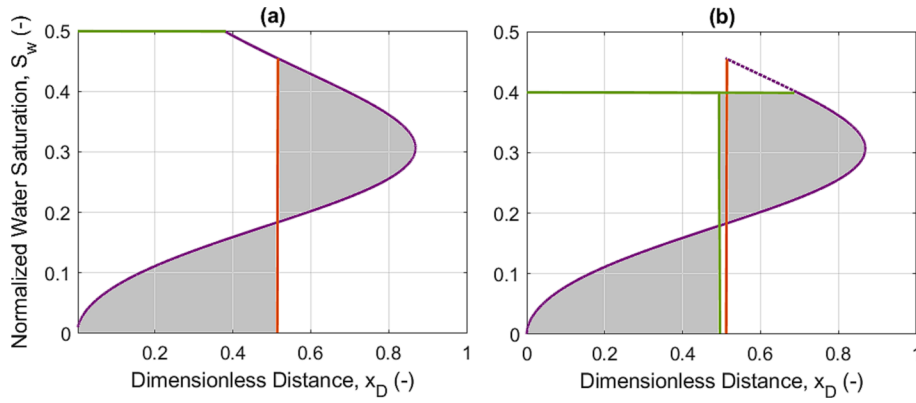
Fig. B1. Illustration of the water saturation distribution in the porous medium when the (a) fractional flow value is higher than the BL saturation front, (b) fractional flow value is lower than the BL saturation front that results in the generation of a Rankine–Hugoniot shock (Rankine, 1870; Hugoniot, 1887).

Now one can consider the interface of two domains as the starting position ($x = 0$) to illustrate the situations if the injection flow flux is not equal to 1.

(a) $S_w(x = 0, t) > S_{wf}$

Considering a constant fractional flow flux (corresponding $S_w = 0.5$ in second domain for example), the water saturation positions calculated from the method of characteristics are shown in Fig. B.1 **(a)**. Clearly, this unphysical solution is resolved by the mass balance between the two grey areas, which results to a same BL front related to $(S_{wf}, f_{S_{wf}})$ on the fractional flow curve.

(b) $S_w(x = 0, t) < S_{wf}$

If a constant lower fractional flow flux is continuously injected at the boundary, the saturation front will be slower than the position of S_{wf} and the front speed will be determined by the Rankine-Hugoniot jump condition:

$$v = \frac{f_{S_{w1}} - f_{S_{w2}}}{S_{w1} - S_{w2}} \tag{B.2}$$

displayed on the graph below (Fig. B.1 **(b)**) with $S_{w1} = 0.4$ and $S_{w2} = 0$.

B.2 - Mathematical formulation

(1) Select saturations to track and calculate breakthrough time to the interface of two domains

Based on the saturation profile developed in the first domain, select representative saturations to track their position and find corresponding saturations in the second domain using the relationship $(f_w)_1 = (f_w)_2$.

The dimensionless breakthrough time to the interface for each saturation in the first domain is given by

$$t_{1,s} = \left(\frac{\partial f_w}{\partial S_w}\right)_{1,S}^{-1} x_{D1} \tag{B.3}$$

where x_{D1} is dimensionless length of the first domain and S represents a given saturation.

Subsequently, check if the saturation is located in the first domain or the second one after comparison of the given time t and $t_{1,s}$.

(2) Calculate the locations of selected saturations for cases 1 and 2.

Case 1. *For a saturation remaining still in the first domain:*

$$x_s = \left(\frac{\partial f_w}{\partial S_w}\right)_{1,S} t \tag{B.4}$$

For a saturation in the second domain:

$$x_s = x_{D1} + \left(\frac{\partial f_w}{\partial S_w}\right)_{2,S} (t - t_{1,s}) \tag{B.5}$$

For a saturation generated in the second domain:
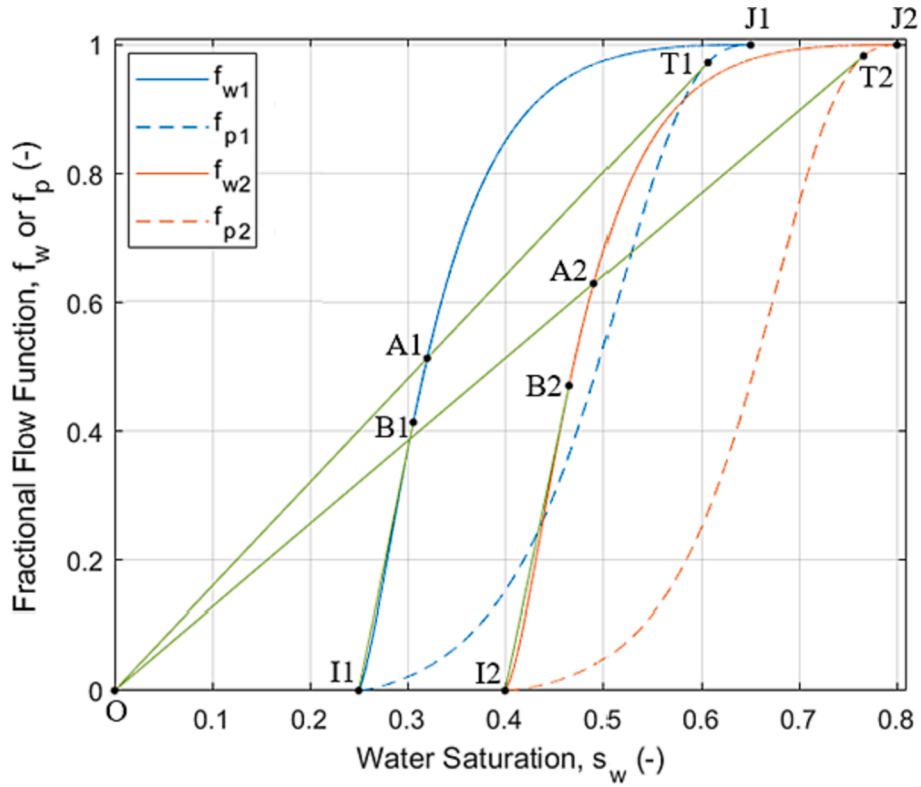
Fig. B2. Tangent lines and points with physical importance displayed on the fractional flow curves of the two-domain composite system.

$$x_s = \left(\frac{\partial f_w}{\partial S_w}\right)_{2,S} t \tag{B.6}$$

Case 2. *For saturations remaining in the first domain, use Eq.* (B.4).

If a constant flow flux flows from the first domain to the second domain, the front velocity is solved by Eq. (B.2) and the location of the front is determined from:

$$x_s = x_{D1} + v_f \left(t - t_{1,s}\right) \tag{B.7}$$

If varied flow fluxes flow from the first domain to the second domain, the saturation front will be continuously overtaken as discussed above. In the second domain, the front velocity should always obey the jump condition (Eq. (B.2)) although the front saturation is dynamically changed. The nearby saturations will catch up with the front saturation due to its higher velocity and the dimensionless fluid velocities of saturation other than the front saturation are still calculated with $\left(\frac{\partial f_i}{\partial S_i}\right)_{2,S}$. After determining the front saturation, the remaining saturation profile in the second domain can be computed by Eq. (B.5).

Note again that polymer profile computation also follows the same procedure as discussed above.

B.3 - Evolution of fractional flow

In this subsection, the detailed evolution of the fractional flow in a heterogeneous system composed of two domains is depicted through a sequence of figures starting from Fig. B.3 and ending in Fig. B.10. Fig. B.2 shows an example of two groups of fractional flow curves (including water–oil and polymer-oil ones) corresponding to the two system domains (domain 1 and domain 2) of the composite system. There are typically four different stages describing the evolution of the fractional flow for either forward (domain 1 to domain 2) or reverse flow (domain 2 to domain 1) direction. Note that in a *n*-domain heterogeneous system, one will need to calculate, plot and follow the described procedure for all *n* distinct fractional flow curves for both water and polymer phases. For the cases shown, chemical retention is considered to be negligible; for cases with chemical retention and inaccessible pore volume, the tangents to the chemical fractional flow curves should be drawn from $\left(-D_{pj} + IPV_j, 0\right)$ for each one of the *j* (= 1,2, ..., *n*) linear beds. Finally, for the cases displayed in Figs. B.2 to B.10 the oil bank water saturation is higher than the water saturation front for the corresponding linear domain. When the water saturation of the oil bank is lower than or equal to the water saturation front, the water saturation will decline sharply from its oil bank value to the initial water saturation for the corresponding linear domain.

Polymer injection from domain 1 to domain 2: In the first stage of the forward case, Fig. B.3 shows that before the waterfront reaches domain 2, the fractional flow of the injected fluid (polymer) is represented only by the fractional flow curves of domain 1. Note that for the water fractional flow curves depicted in Fig. B.3, the waterfront saturation is lower than the water saturation in the formed oil banks. The fluids saturations across the formations are described by the flow path ***J1-T1-A1-B1-I1-I2*** depicted in Fig. B.3. When the water front breaks through the interface between the two
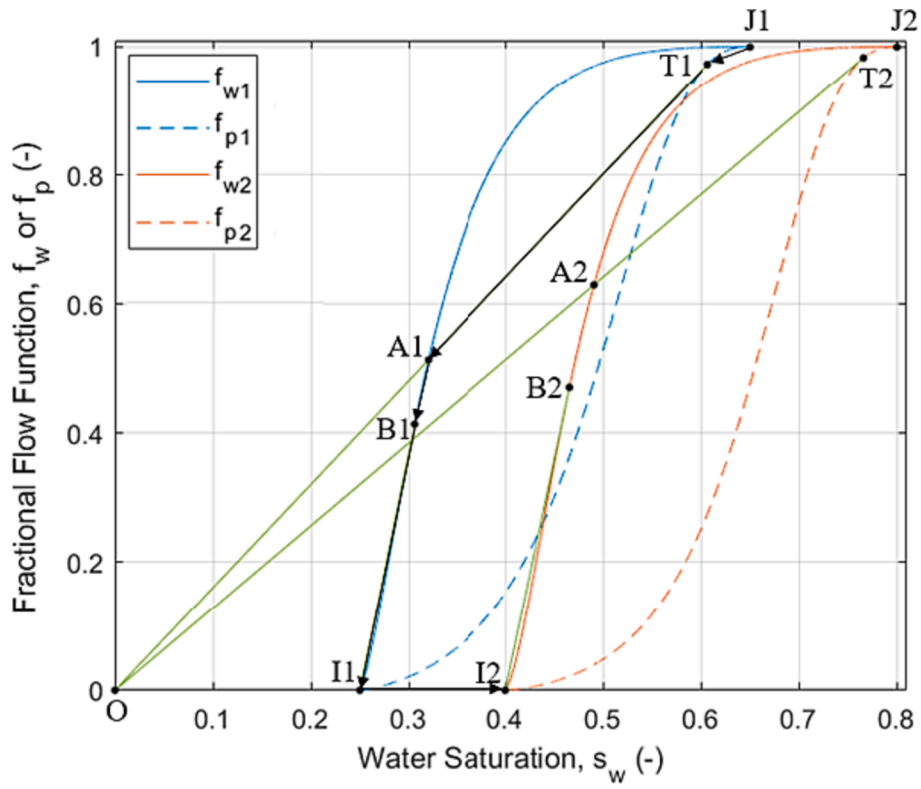
Fig. B3. First stage - Prior to water and polymer saturations reaching the interface between the two domains in the composite system, the fractional flow of the injected fluid is only related to the fractional flow curves of domain 1.
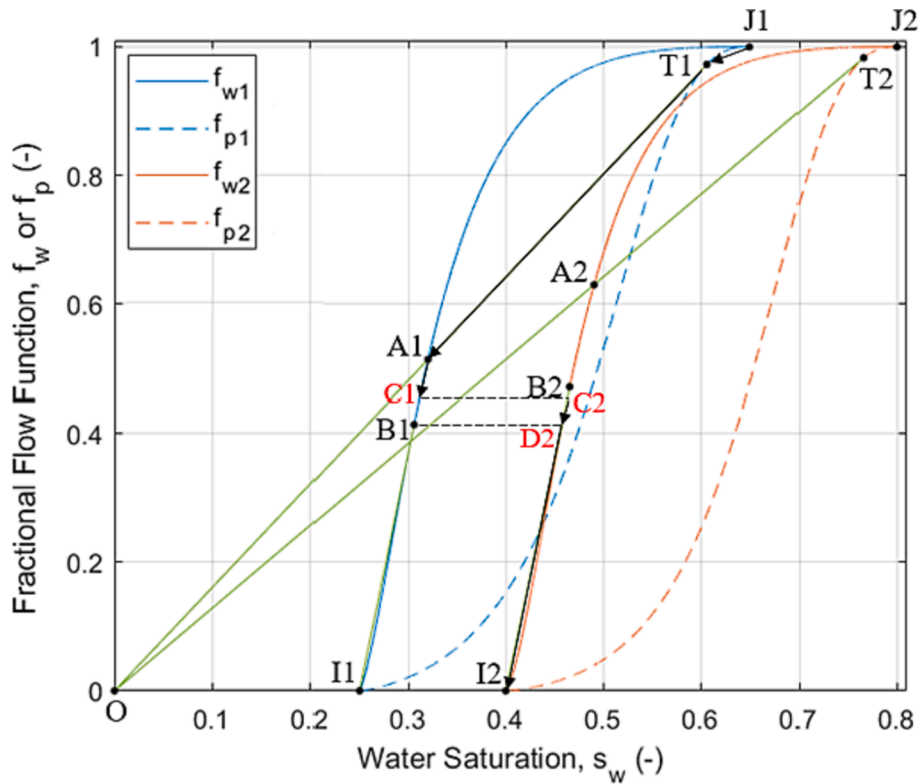
Fig. B4. Second stage - The BL front of domain 1 passes to domain 2 and the corresponding water fractional flow curve generates lower water saturations than the BL front saturation of domain 2. The velocity of the waterfront in domain 2 follows the Rankine-Hugoniot jump condition (Eq. (B.2) and the BL saturation will eventually take over the waterfront due to its higher velocity.
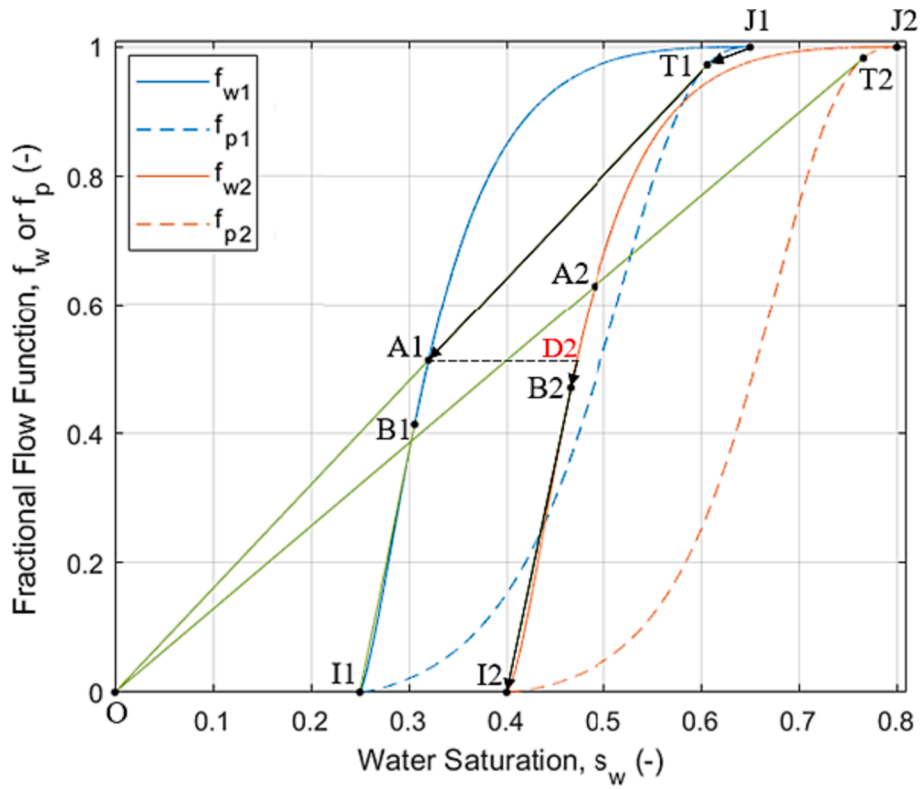
Fig. B5. Third stage - All the variable water saturations passed over the domain 1. An oil bank saturation 1-s_{wD2} is formed in domain 2 where the BL front saturation s_{wB2} may turn to new waterfront saturation.
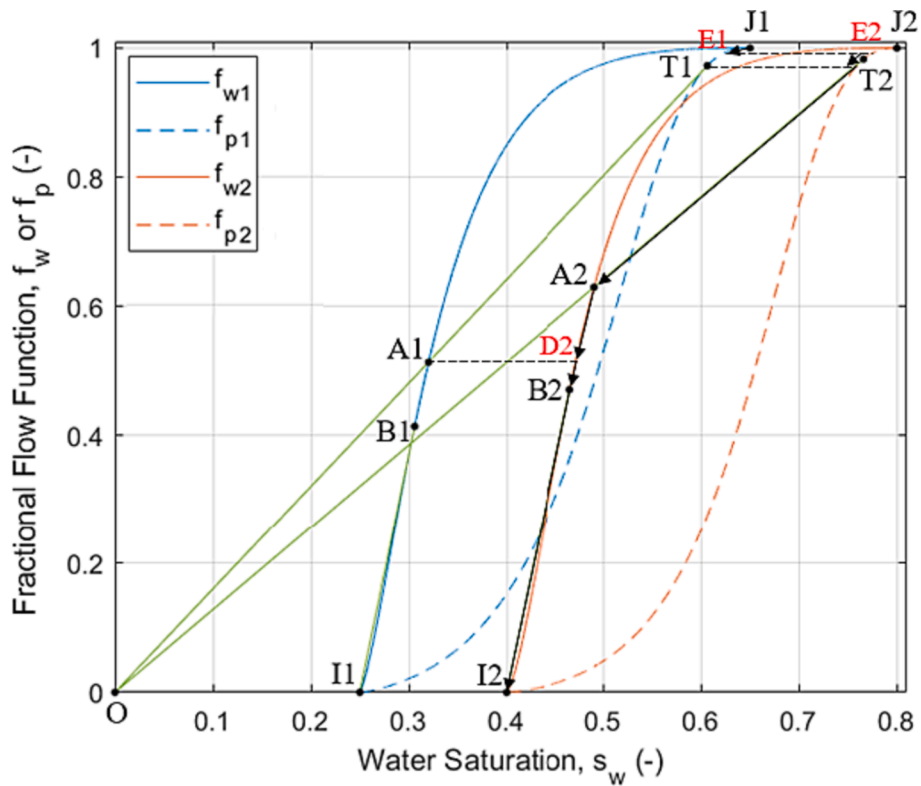
Fig. B6. Fourth stage - Polymer front reaches to domain 2 where a new oil bank saturation 1-s_{wA2} is generated just ahead of polymer front. There is a saturation jump (A2-D2) between the new and old oil bank saturations (1-s_{wA2} and 1-s_{wD2}).
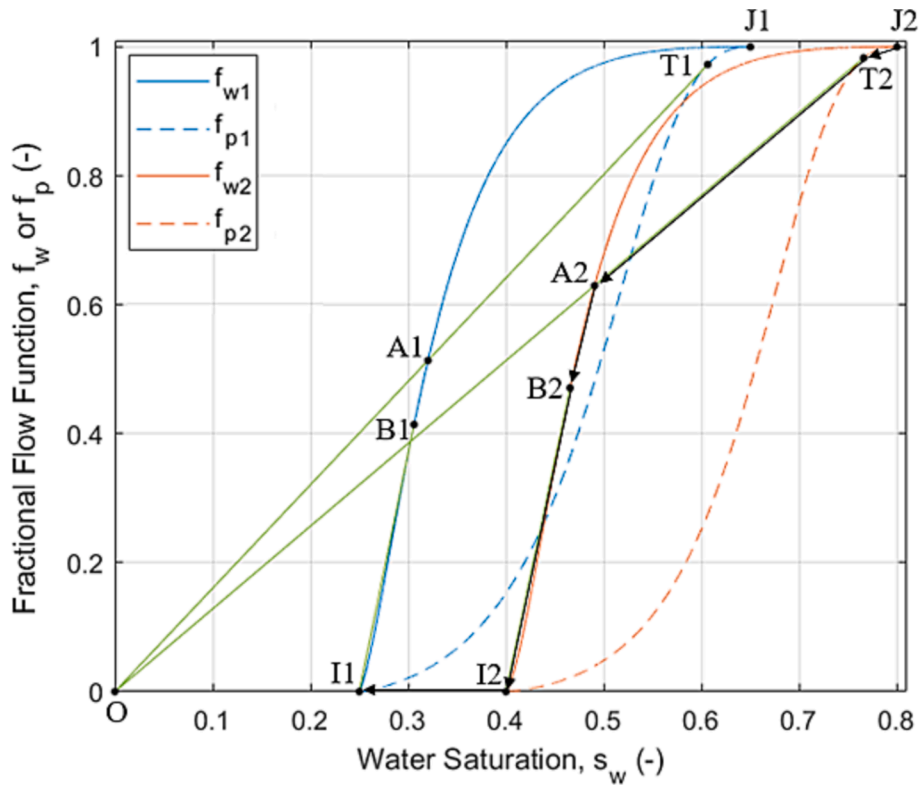
Fig. B7. First stage - Prior to water and polymer saturations reaching the interface between the two domains in the composite system, the fractional flow of the injected fluid is only related to the fractional flow curves of domain 2.
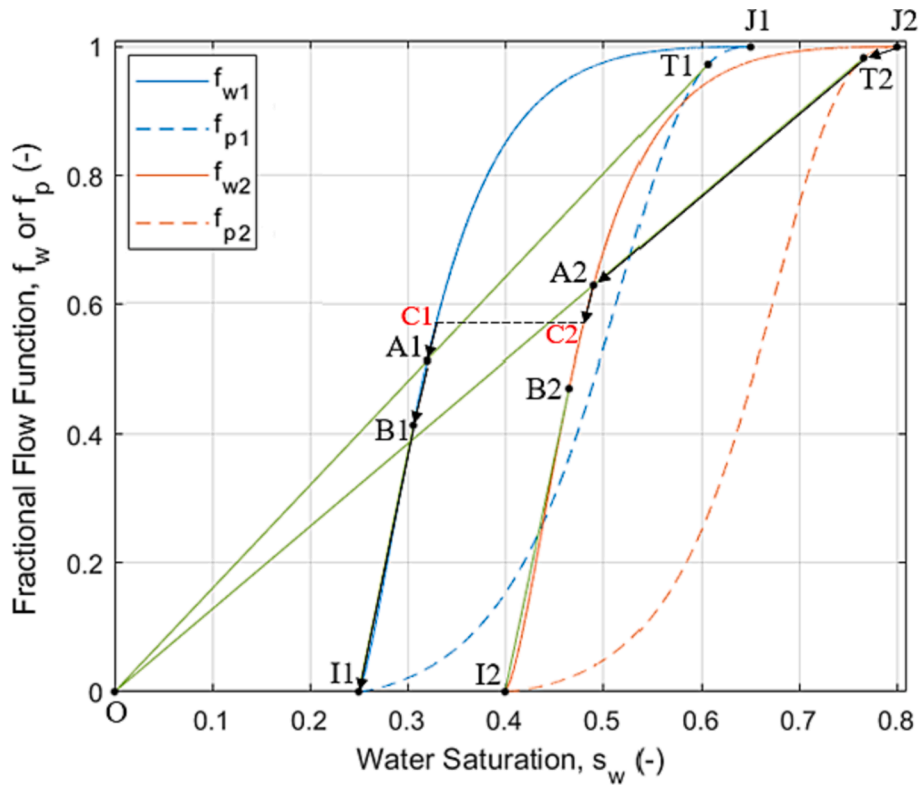
Fig. B8. Second stage - The BL front of domain 2 passes to domain 1 and the corresponding water fractional flows generate the BL front saturation profile (C1-B1) in domain 1.
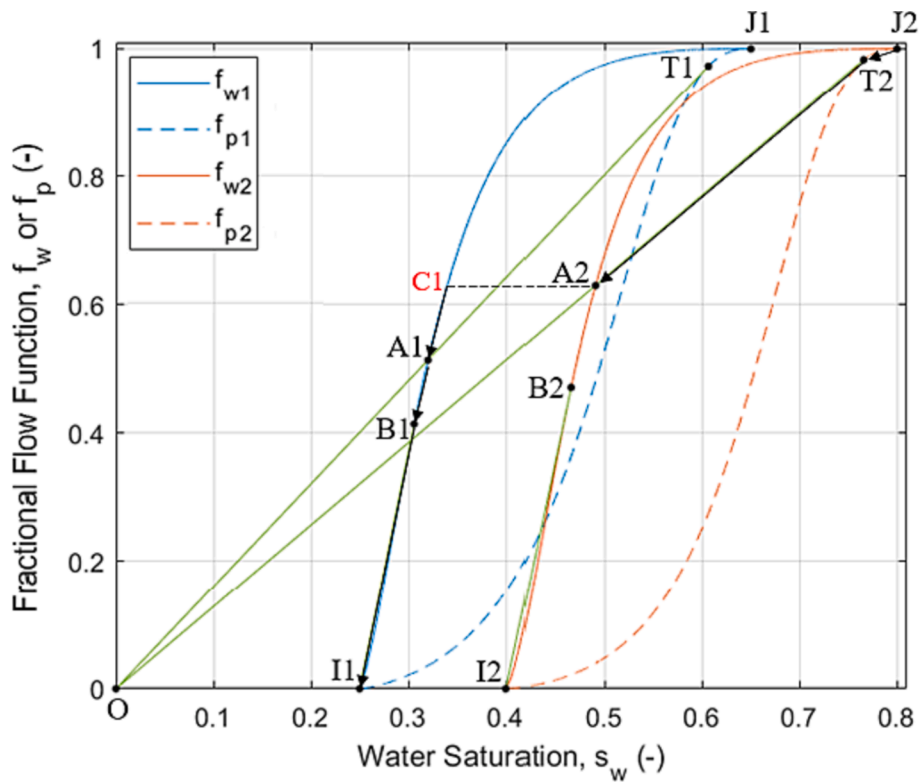
Fig. B9. Third stage - All the variable water saturations passed over the domain 2. An oil bank is formed in domain 1 with saturation 1-s_{wC1}.
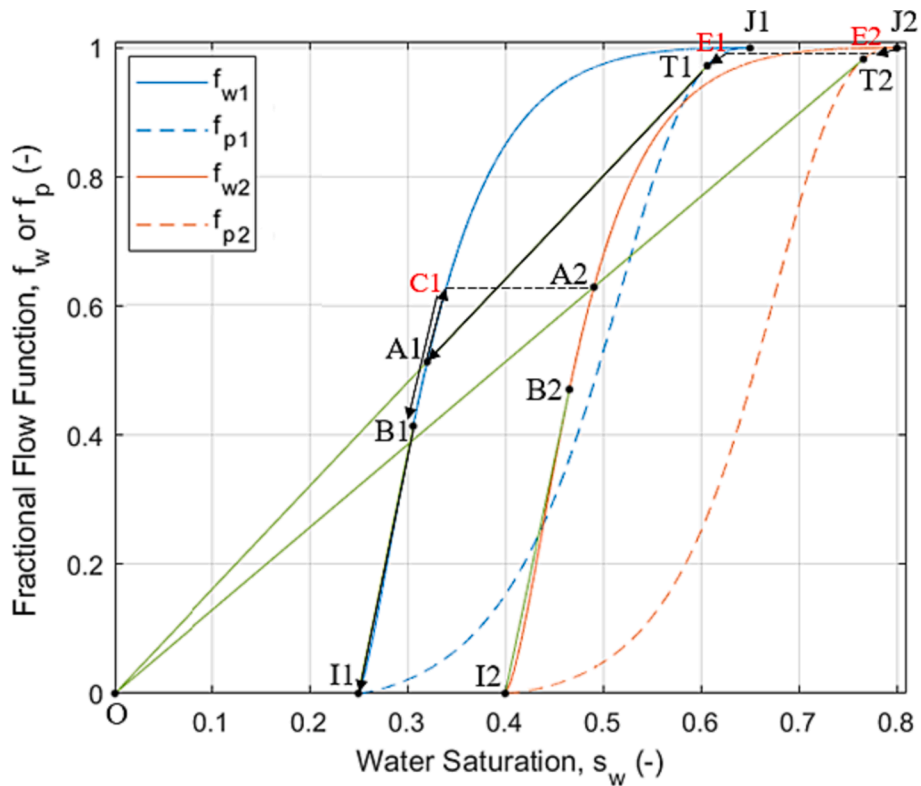
Fig. B10. Fourth stage - Polymer front reaches to domain 1 where a new oil bank saturation 1-s_{wA1} is generated just ahead of polymer front. There is a water saturation jump (A1-C1) between the new and old oil bank water saturations (s_{wA1} and s_{wC1}).

formation domains, the water fractional flow **C1-B1** in domain 1 (shown in Fig. B.4) will transfer to **C2-D2** in domain 2 with different water saturation values, and it will therefore develop a new water front saturation s_{wD2} which is lower than the BL front saturation s_{wB2}, which is the second stage of fractional flow path (**J1-T1-A1-C1-C2-D2-I2**). The velocity of new waterfront saturation s_{wD2} is slower than the nearby saturations and therefore the front saturation will increase to s_{wB2}. Eventually, all the varied water saturations (**A1-B1**) in domain 1 will pass to domain 2. Fig. B.5 exactly shows the corresponding aqueous fractional flow path (**J1-T1-A1-D2-B2-I2**) at the third stage and the oil bank saturation $1-s_{wA1}$ in domain 1 shifts to $1-s_{wD2}$ in domain 2. Note that here we assume that at the end of the second stage the BL front saturation in domain 2 has already been developed to be s_{wB2}. Otherwise, there will still be a water saturation profile with lower saturation values than s_{wB2}. At the end of the process (i.e., fourth stage), the oil bank region in domain 1 will fully pass into domain 2 and at the same time the polymer in domain 1 enters into the domain 2. The path that describes the fluids saturation in the entire system is associated with the curve **J1-E1-E2-T2-A2-D2-B2-I2** displayed in Fig. B.6. In particular, at the third stage the oil bank saturation is $1-s_{wD2}$ in domain 2 and when polymer enters the domain 2 at the fourth stage a new oil bank saturation $1-s_{wA2}$ is formed and will propagate in the domain 2, which will result in an oil saturation jump or shock from $1-s_{wA2}$ to $1-s_{wD2}$ (see formation saturation profile at t 25 min displayed in Fig. 20) with a velocity computed through the Rankine-Hugoniot jump condition (Eq. (B.2)).

Polymer injection from domain 2 to domain 1: In the first stage of the reverse flow direction case, Fig. B.7 shows that before the waterfront reaches the domain 1, the fractional flow of the injected fluid (polymer) is represented only by the fractional flow curves of domain 2. The fluids saturations across the formations are described by the flow path **J2-T2-A2-B2-I2-I1** depicted in Fig. B.7. When the water front breaks through the interface between the two formation domains, the water fractional flow **C2-B2** in domain 2 (shown in Fig. B.8) will transfer to **C1-B1** in domain 1 with different water saturation values, and it will therefore develop the BL saturation profile (**C1-B1**), which is the second stage of fractional flow path (**J2-T2-A2-C2-C1-A1-B1-I1**). Eventually, all the varied water saturations (**A2-B2**) in domain 2 will pass into the domain 1. Fig. B.9 exactly shows the corresponding aqueous fractional flow path (**J2-T2-A2-C1-A1-B1-I1**) at the third stage and the oil bank saturation $1-s_{wA2}$ in domain 2 shifts to $1-s_{wC1}$ in domain 1. At the end of the process (i.e., fourth stage), the oil bank region in domain 2 will totally pass into domain 1 and at the same time the polymer in domain 2 enters the domain 1. The path that describes the fluids saturation in the entire system is associated with the curve **J2-E2-E1-T1-A1-C1-B1-I1** displayed in Fig. B.10. Specially, at the third stage the oil bank saturation is $1-s_{wC1}$ in domain 1 and when polymer enters into the domain 1 at the fourth stage a new oil bank saturation $1-s_{wA1}$ is generated and will propagate in the domain 1, which will result in an oil saturation jump or shock from $1-s_{wA1}$ to $1-s_{wC1}$ with a velocity computed through the Rankine-Hugoniot jump condition (Eq. (B.2)).

References

Askarinezhad, R., Hatzignatiou, D.G., and Stavland, A. 2017. Associative Polymers as Enhanced Oil Recovery Agents in Oil-Wet Formations: A Laboratory Approach, EAGE paper, IOR NORWAY 2017 - 19th European Symposium on Improved Oil Recovery, Stavanger, Norway, 24-27 April. https://www.earthdoc.org/content/papers/ 10.3997/2214-4609.201700275.

Askarinezhad, R., Hatzignatiou, D.G., and Stavland, A. 2018. Core-Based Evaluation of Associative Polymers as Enhanced Oil Recovery Agents in Oil-Wet Formations. *ASME J. of Energy Resources Technology*, 140 (3), 032915-1 – 032915-9, JERT-17-1418. 10.1115/1.4038848.

Askarinezhad, R., Hatzignatiou, D.G., Stavland, A., 2021. Associative polymers for disproportionate permeability reduction – formation wettability effects. J. of Petr. Sci. & Eng. 206, 109060 https://doi.org/10.1016/j.petrol.2021.109060.

Azad, M.S., Trivedi, J.J., 2018. Understanding the flow behavior of copolymer and associative polymer using extensional viscosity characterization: effect of hydrophobic association. Can. J. Chem. Eng. 96, 2498–2508. https://doi.org/10.1002/cjce.23169.

Buckley, S.E., Leverett, M.C., 1942. Mechanism of fluid displacement in sands. Trans AIME 146, 107–116.

Carreau, P.J., 1972. Rheological equations from molecular network theories. Trans. Soc. Rheolog. 16 (1), 99–127.

CMG Computer Modelling Group, 2021. STARS User Guide. STARS 2021, 10.

Ding, L., Wu, Q., Zhang, L., et al., 2020. Application of fractional flow theory for analytical modeling of surfactant flooding, polymer flooding, and surfactant/polymer flooding for chemical enhanced oil recovery. Water 12 (8), 2195.

Erincik, M.Z., Qi, P., Balhoff, M.T., and Pope, G.A. 2017. New Method to Reduce Residual Oil Saturation by Polymer Flooding. Paper SPE-187230-MS presented at SPE Annual Technical Conference and Exhibition, San Antonio, Texas, USA, 9-11 October. 10.2118/187230-MS.

Green, D.W., Willhite, G.P., 1998. Enhanced Oil Recovery. Doherty Memorial Fund of AIME, Society of Petroleum Engineers, Richardson, Texas, Henry L.

Hatzignatiou, D.G., Norris, U.L., Stavland, A., 2013. Core-scale simulation of polymer flow through porous media. J. of Pet. Sci. & Eng. 108, 137–150. https://doi.org/10.1016/j.petrol.2013.01.001.

Hatzignatiou, D.G., Moradi, H., Stavland, A., 2015. Polymer flow through water- and oil-wet porous media. J. Hydrodyn. 27 (5), 748–762. https://doi.org/10.1016/S1001-6058(15)60537-6.

Herschel, W.H., Bulkley, R., 1926. Konsistenzmessungen Von Gummi-Benzollosungen. Kolloid-Zeitschrift 39, 291–300. https://doi.org/10.1007/BF01432034.

Hugoniot, H., 1887. Mémoire sur la propagation des mouvements dans les corps et spécialement dans les gaz parfaits (première partie) [Memoir on the propagation of movements in bodies, especially perfect gases (first part)]. J. De L'école Polytech. (in French). 57, 3–97.

Huh, C. and Pope, G.A. 2008. Residual Oil Saturation from Polymer Floods: Laboratory Measurement and Theoretical Interpretation. Paper SPE-113417 presented at 2008 SPE/DOE Improved Oil Recovery Symposium, Tulsa, 19 – 23 April. 10.2118/113417-MS.

Lotfollahi, M., Koh, H., Li, Z., Delshad, M., and Pope, G. 2016. Mechanistic Simulation of Residual Oil Saturation in Viscoelastic Polymer Floods. Paper SPE-178844-MS presented at the SPE EOR Conference at Oil and Gas West Asia, Muscat, Oman, 21–23 March. 10.2118/179844-MS.

Ostwald, 1929. De waele-ostwald equation. Kolloid Z. 47, 176–187.

Qi, P., Lashgari, H., Luo, H., Delshad, M., Pope, G., and Balhoff, M. 2018. Simulation of Viscoelastic Polymer Flooding—From the Lab to the Field. Paper SPE-191498-MS presented at the SPE Annual Technical Conference and Exhibition, Dallas, Texas, USA, September 2018. 10.2118/191498-MS.

Qiao, Y. and Hatzignatiou, D.G. 2023. Analytical Solutions of Viscoelastic Polymer Injection in Heterogeneous Porous Media. Paper in preparation.

Rankine, W.J.M., 1870. On the thermodynamic theory of waves of finite longitudinal disturbances. Philos. Trans. R. Soc. Lond. 160, 277–288.

Rossen, W.R., Venkatraman, A., Johns, R.T., et al., 2011. Fractional flow theory applicable to non-newtonian behavior in EOR processes. Transp. Porous Media 89 (2), 213–236.

Song, W., Hatzignatiou, D.G., 2022. On the Reduction of the Residual Oil Saturation through the Injection of Polymer and Nanoparticle Solutions. J. of Petr. Sci. & Eng. 208, Part B, 109430 https://doi.org/10.1016/j.petrol.2021.109430.

Sorbie, K.S., 1991. Polymer-improved oil recovery. Blackie and Sons Ltd., Glasgow, Scotland.

Sun, L., Li, B., Jiang, H., Li, Y., Jiao, Y., 2019. An injectivity evaluation model of polymer flooding in offshore multilayer reservoir. Energies 12, 1444.

Wang, D., Xia, H., Liu, Z. and Yang Q. 2001. Study of the Mechanism of Polymer Solution with Visco-Elastic Behavior Increasing Microscopic Oil Displacement Efficiency and the Forming of Steady "Oil Thread" Flow Channels. Paper SPE 68723 presented at the SPE Asia Pacific Oil and Gas Conference and Exhibition, 17 April, Jakarta, Indonesia. DOI: 10.2118/68723-MS.

Welge, H.J., 1952. A simplified method for computing oil recovery by gas or water drive. Trans. AIME 3, 108.

Wu, Y.S., 2016. Multiphase fluid flow in porous and fractured reservoirs. Elsevier.

Wu, Y.S., Fakcharoenphol, P., and Zhang R.L. 2010. Non-Darcy Displacement in Linear Composite and Radial Flow Porous Media. Paper SPE 130343 presented at the SPE EUROPEC/EAGE Annual Conference and Exhibition, 14–17 June, Barcelona, Spain. DOI: 10.2118/130343-MS.

Wu, Y.S., Pruess, K., Witherspoon, P.A., 1991. Displacement of a newtonian fluid by a non- newtonian fluid in a porous medium. Transp. Porous Media 6, 115–142.

Wu, Y.S., Pruess, K., Chen, Z.X., 1993. Buckley-Leverett flow in composite porous media. SPE Adv. Technol. Ser. 1 (02), 36–42.